



Lab on a Chip

A review of optoelectrowetting (OEW): from fundamentals to lab-on-a-smartphone (LOS) applications to environmental sensors

Journal:	<i>Lab on a Chip</i>
Manuscript ID	LC-ART-04-2022-000372.R1
Article Type:	Critical Review
Date Submitted by the Author:	21-Jul-2022
Complete List of Authors:	Thio, Si Kuan; National University of Singapore, Mechanical Engineering Park, Sung-Yong; San Diego State University, Mechanical Engineering

SCHOLARONE™
Manuscripts

CRITICAL REVIEW

A review of optoelectrowetting (OEW): from fundamentals to lab-on-a-smartphone (LOS) applications to environmental sensors

Si Kuan Thio ^a and Sung-Yong Park ^{*b}

Received 00th January 20xx,
Accepted 00th January 20xx

DOI: 10.1039/x0xx00000x

Electrowetting-on-dielectric (EWOD) has been extensively explored as an active-type technology for small-scale liquid handling due to its several unique advantages, including no requirement of mechanical components, low power consumption, and rapid response time. However, conventional EWOD devices are often accompanied with complex fabrication processes for patterning and wiring of 2D arrayed electrodes. Furthermore, their sandwiched device configuration makes the difficulty in integrating with other microfluidic components. More recently, optoelectrowetting (OEW), a light-driven mechanism for effective droplet manipulation, has been proposed as an alternative approach to overcome these issues. By utilizing optical addressing onto a photoconductive surface, OEW can dynamically control an electrowetting phenomenon without the need for complex control circuitry on a chip, while providing higher functionality and flexibility. Using commercially available spatial light modulators such as LCD display and smartphone, millions of optical pixels are readily generated to modulate virtual electrodes for large-scale droplet manipulations in parallel on low-cost OEW devices. The benefits of the OEW mechanism have seen it being variously explored in its potential biological and biochemical applications. This review article presents the fundamentals of the OEW, discusses its research progresses and limitations, highlights various technological advances and innovations, and finally introduces the emergence of the OEW technology as portable smartphone-integrated environmental sensors.

1. Introduction

Droplet-based microfluidic systems have attracted significant interests for various lab-on-a-chip (LOC) applications in past decades.¹⁻⁴ By manipulating discrete droplets of biological and chemical reagents in an immiscible phase, droplet-based microfluidic devices offer several advantages over single-phase continuous systems, such as rapid mixing, reagent transport without dispersion, and minimization of cross contamination issues between droplets.⁵⁻⁷ With these benefits, numerous applications have been demonstrated on droplet-based microfluidic devices, including single-cell encapsulation,⁸⁻¹¹ pathogenic bacteria detection¹²⁻¹⁴ and polymerase chain reactions (PCR) for DNA amplification.¹⁵⁻¹⁷ One drawback associated with such droplet-based microfluidic systems is the difficulty to handle individual droplets driven by a continuous oil flow confined along microfluidic channels.¹⁸⁻²⁰ To overcome this challenging issue, various active-type droplet manipulation mechanisms have been extensively developed, such as dielectrophoresis (DEP),²¹⁻²³ electrowetting on dielectric (EWOD),²⁴⁻²⁷ thermocapillary force,²⁸⁻³⁰ and magnetic force.³¹⁻³³

Among these techniques, EWOD technology has been widely developed for active droplet control. It offers several unique advantages over other active-type mechanisms,

including (1) no mechanical components (e.g., pumps or valves) required for fluidic actuation, (2) extremely low power consumption (in the range of $\sim\mu\text{W}$), and (3) rapid response time in milliseconds. A wide range of applications have been demonstrated, including lab-on-a-chip,³⁴⁻³⁶ tunable optics,³⁷⁻³⁹ thermal cooling of microdevice,^{40, 41} and energy harvesting⁴²⁻⁴⁶ using EWOD technology. In recent years, many researchers have investigated on optical control of the EWOD mechanism, called optoelectrowetting (OEW) for effective droplet manipulations with the benefits of device simplicity, reconfigurability, flexibility, and functionality.⁴⁷⁻⁵⁰ Since light can be flexibly patterned and reconfigured on a photoconductive surface of OEW devices, an electrowetting phenomenon can be dynamically controlled without the need for complex control circuitry on a chip typically required for EWOD devices. Using commercially available spatial light modulators such as liquid crystal display (LCD), digital micromirror device (DMD), and smartphone, millions of optical pixels are readily generated to modulate virtual electrodes in parallel on low-cost devices. A variety of applications have been involved with the OEW technologies, such as droplet dispensing and merging,^{51, 52} integrated biosensing devices,^{53, 54} smartphone-based detection of water quality,^{55, 56} as well as biochemical and cell analyses.^{57, 58}

This review paper highlights technological advances of OEW and their applications as smartphone-integrated biosensors. Since early OEW devices imitated EWOD, the basic concept of the EWOD mechanism is first described in Chapter 2. We further discuss about the fundamentals of the OEW

^a Department of Mechanical Engineering, National University of Singapore, 9 Engineering Drive 1, Singapore, 117575.

^b Department of Mechanical Engineering, San Diego State University, 5500 Campanile Drive, San Diego, CA, USA, 92182.

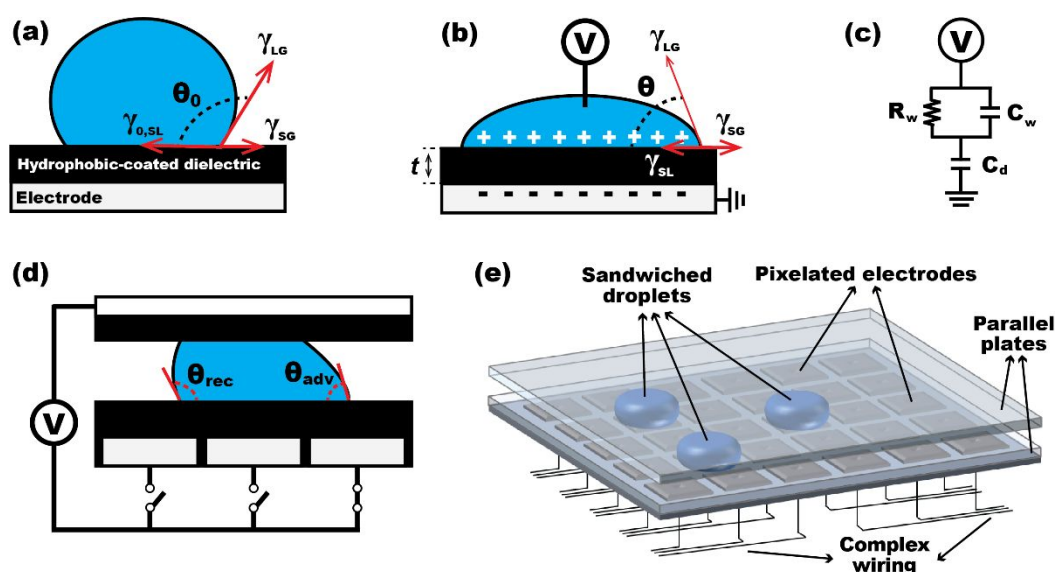


Fig. 1 A working principle of the electrowetting on dielectric (EWOD) for droplet actuation. (a) When a liquid droplet is placed on a solid surface, it forms an initial contact angle (θ_0) along a three-phase contact line at the equilibrium where three surface tension forces of γ_{SL} , γ_{SG} and γ_{LG} at the solid-liquid (SL), solid-gas (SG), and liquid-gas (LG) interfaces are balanced. (b) With an electric potential applied between the liquid droplet and electrode plate, the electric charges are re-distributed and modify the surface tension at the solid-liquid interface, resulting in a decrease in the droplet contact angle. (c) An equivalent circuit model consists of two electric impedances of liquid droplet and dielectric layers. (d) To actuate a droplet, a bias voltage is applied between the top electrode plate and the bottom pixelated electrode nearby the droplet. Then, it forms an advancing contact angle (θ_{adv}) at the electrically activated electrode and a receding angle (θ_{rec}) at the other side. This creates a pressure gradient inside the droplet and drives it towards the region electrically activated. (e) Conventional EWOD devices typically encounter the issues of complex fabrication processes for patterning and wiring of 2D arrayed electrodes.

technology to explain how an OEW-based droplet actuation principle works differently from the EWOD. Research progress and limitations on different types of OEW technologies and devices are detailed in Chapter 3. In Chapter 4, further developments and technological innovations in the OEW are presented. Finally, the emergence of OEW technology as smartphone-integrated portable biosensors are introduced in Chapter 5. A brief comparison of these OEW technologies and devices is also summarized in Table 1.

2. Fundamentals of EWOD and OEW

2.1 EWOD-based droplet actuation

Since Lippmann's first study in 1875,⁵⁹ electrowetting (EW) has been extensively explored as an effective means for small-scale liquid handling due to the dominance of surface tension forces over body forces in micro/meso scales. When an electric potential is applied between a liquid droplet and a solid electrode, the electric charges are re-distributed to modify the surface tension at the liquid-solid interface, where the like-charge repulsion decreases the work by expanding the surface area. The resulting contact angle (θ) of a liquid droplet can be mathematically estimated using the Young-Lippmann equation as:^{60, 61}

$$\cos \theta = \cos \theta_0 + \frac{c_d (\Delta V)^2}{2\gamma_{LG}} \quad (1)$$

where θ_0 is an initial contact angle of the droplet with zero potential application, γ_{LG} is the surface tension between two immiscible fluids (i.e., the liquid droplet and its surrounding medium), c_d is the capacitance of a dielectric layer per unit area, and ΔV indicates the voltage drop across a dielectric capacitor.

Conventional EW uses electrolytes in a direct contact with a solid electrode, where an electric double layer capacitor (EDLC) is formed to hold the storage energy induced by applying an electric potential. However, the thickness of the EDLC is typically very thin (less than 10 nm), and susceptible to electric breakdown.^{61, 62} As a result, contact angle modulation of a droplet was seriously limited in conventional EW as the process is irreversible after electric breakdown. Later, the principle of electrowetting-on-dielectric (EWOD) was implemented to overcome this prevalent issue.⁶³⁻⁶⁵ With EWOD, large contact angle modulation can be achieved by replacing the EDLC with a thin dielectric layer between the liquid and the electrode, due to its ability to hold large electrostatic energy.^{66, 67} Furthermore, adding a hydrophobic coating to the dielectric layer can provide large initial surface energy and high reversibility.²⁴

Fig. 1 presents a working principle of the EWOD mechanism for droplet actuation. A liquid droplet sits on a hydrophobic-coated dielectric layer below which an electrode plate is placed (Fig. 1a). The droplet forms its initial contact angle (θ_0) along a three-phase contact line at the equilibrium where three surface tension forces (i.e., $\gamma_{SL,0}$, γ_{SG} , and γ_{LG}) are balanced. When a bias voltage is applied between the droplet

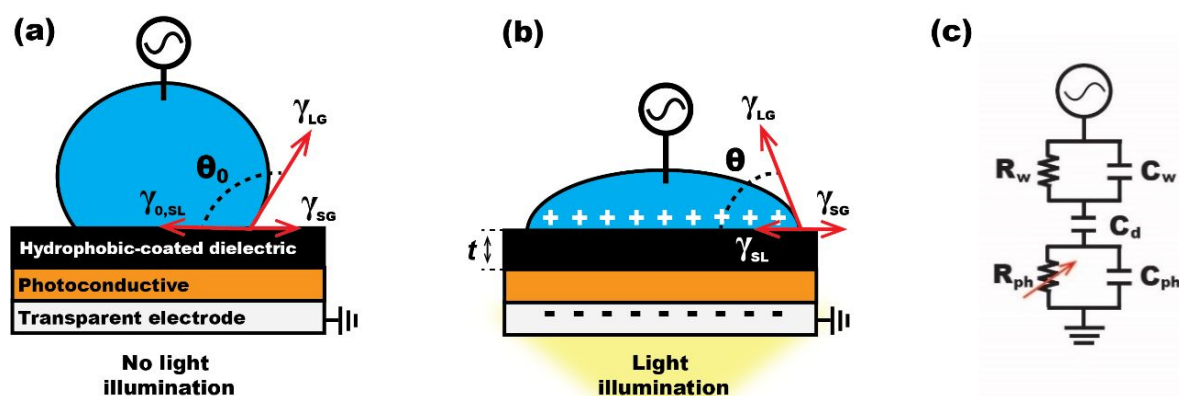


Fig. 2 A working principle of the optoelectrowetting (OEW) for optical droplet actuation. (a) An OEW device is composed of a hydrophobic-coated dielectric and an electrode. With an AC voltage applied between the liquid droplet and the bottom electrode, it forms its initial contact angle (θ_0) on the solid surface under a dark state (i.e., no light illumination) (b) Upon the illumination of light from the bottom, the dominance of the electric impedance shifts from the photoconductive layer to the dielectric layer due to the increase in its conductivity. As a result, most of the voltage drop is created across the dielectric layer. This induces an electrowetting effect by decreasing the liquid droplet's contact angle to θ . (c) An equivalent circuit model of the OEW consisting of three electric impedances across liquid droplet, dielectric, and photoconductive layers.

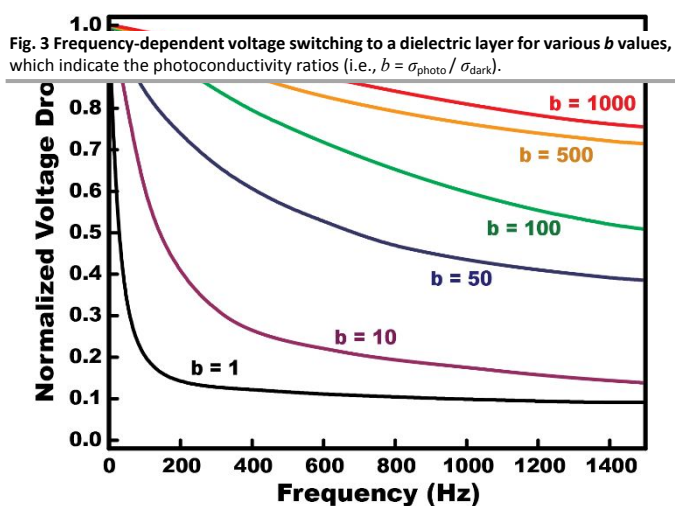
and the bottom electrode, the electric energy, $c(\Delta V)^2/2$, is stored across the dielectric capacitor (c_d). This storage energy makes the electric charges re-distribute at the liquid-solid interface and decreases the surface tension force from $\gamma_{0,SL}$ to γ_{SL} . This force modification leads to the contact angle change of the droplet from θ_0 to θ (Fig. 1b). Fig. 1(c) shows an equivalent circuit consisting of two electric impedances across a liquid droplet and a dielectric layer serially connected.

To accomplish droplet actuation, an EWOD mechanism utilizes such an electrically controlled contact angle of the droplet on a solid surface. As illustrated in Fig. 1(d), a conventional EWOD device consists of two parallel plates sandwiching a liquid droplet in between. The top plate is a hydrophobic-coated electrode, while the bottom plate is composed of 2D arrayed pixelated electrodes covered with a hydrophobic-coated dielectric layer.⁶⁸⁻⁷¹ To actuate a droplet on an EWOD device, an electric potential is applied between the top electrode plate and the bottom pixelated electrode nearby the droplet. The droplet's contact angle correspondingly decreases to form an advancing angle (θ_{adv}) on the electrically activated electrode and a receding angle (θ_{rec}) at the other side (Fig. 1d). Consequently, a pressure gradient is created inside the droplet and drives it towards the region electrically activated. To further implement droplet transportation, the foregoing steps are repeated by sequentially activating nearby electrodes. Thus, conventional EWOD devices are appended with several drawbacks. Firstly, the minimum droplet size that can be manipulated on a device relies on the size of the physically pixelated electrode, limiting device versatility and reconfigurability. Moreover, conventional EWOD devices come with the drawback of device complexity led by complex electrode patterning and wiring issues (Fig. 1e). While the process of pixelated electrode patterning can be simplified with the use of printed circuit boards (PCBs), a tedious process of

connecting each individual electrode to a wire may lead to potential interconnection problems.⁷² Such problems can prove to be particularly susceptible when fabricating an EWOD device where large-scale parallel manipulations of multiple droplets are required. These issues can be further eliminated with wiring connection by the via process, ultimately increasing the fabrication cost and complexity of an EWOD device.⁷³

2.2 OEW-based droplet actuation

On the other hand, optoelectrowetting (OEW) technologies have been proposed as alternative solutions to address these fabrication issues arisen from conventional EWOD devices. Instead of electric activation of individual electrodes on EWOD, OEW makes use of optical addressing on a photoconductive surface to induce an electrowetting effect. Fig. 2(a) shows the structure of a typical OEW device. The main distinction from EWOD is the use of a photoconductive layer between a hydrophobic-coated dielectric layer and a bottom electrode. An equivalent circuit model of the OEW shown in Fig. 2(c) can be used to understand how an electrowetting effect (i.e., contact angle change of the droplet) can be induced by light illumination. It can be equivalently modelled to have three electric impedances across the layers of a liquid droplet, a dielectric, and a photoconductor, which are serially connected. To achieve droplet actuation, an alternating current (AC) voltage is applied between the liquid droplet and the bottom electrode. However, the droplet remains close to its initial contact angle on the solid surface under a dark state (i.e., no light illumination), as illustrated in Fig. 2(a). This is because majority of the voltage drop is occurring across the photoconductive layer where electric impedance is dominant. Hence, a very small amount of the voltage drop is created across the capacitance (c_d) of the dielectric layer, and the contact angle



remains almost unchanged as the initial value (θ_0). To induce an OEW effect, light illuminates onto a photoconductive layer after passing through a transparent electrode from the bottom (Fig. 2b). This generates excess electron-hole pairs at the illuminated area, leading to an increase in the photoconductivity by several orders. As a result, the electric impedance of the photoconductive layer significantly decreases to switch the dominance of the voltage drop (ΔV) in the dielectric layer. Correspondingly, the droplet's contact angle becomes lowered as estimated by the Young-Lippmann Eq. (1).

It is worthwhile to note that this light-enabled voltage switching effect relies on the frequency of an applied AC voltage. Using the equivalent circuit model presented in Fig. 2 (c), we have studied the frequency-dependent voltage drop normalized to the input voltage. For this study, it was assumed that the thicknesses of water, dielectric, and photoconductive layers are 200 μm , 1 μm and 5 μm , respectively. An electric conductivity of a photoconductive layer was set to be $\sigma_{\text{dark}} = 1.6 \times 10^{-6} \text{ S/m}$ at a dark state. Fig. 3 presents the normalized voltage drop across a dielectric layer as a function of the AC frequency for various photoconductivity ratios between illuminated and dark states (i.e., $b = \sigma_{\text{photo}} / \sigma_{\text{dark}}$). At the frequencies below 50 Hz, majority of the voltage drop is created in a dielectric layer even under a dark state (i.e., $b = 1$). Therefore, effective OEW modulation can't be achieved for optical droplet actuation. For the frequencies above 200 Hz, only a small amount of the voltage drops across the dielectric layer in a dark state. However, when light illuminates onto a photoconductive layer (i.e., $b > 1$), its conductivity increases to switch the dominance of the voltage drop to the dielectric layer. This voltage switching effect continues to enlarge with the light intensity illuminated (see Fig. 3). For example, at the AC frequency of 200 Hz, only 13% of the input voltage drops across the dielectric layer under a dark state, leading to a negligible contact angle change. However, when light illuminates with the photoconductivity

ratio of $b = 100$, about 90% of the input voltage can be stored across the dielectric layer to contribute to OEW modulation even at the same input frequency of 200 Hz. This voltage switching effect makes significant modification in the droplet's contact angle to be used for optical droplet actuation. Another interesting observation from Fig. 3 is that the voltage switching effect begins to saturate when $b > 500$ where the electric impedance of the photoconductive layer become negligible.

To achieve droplet transportation, the OEW utilizes sequential addressing of a light pattern onto a continuously deposited (i.e., no patterned) photoconductive surface, instead of sequential activation on pixelated electrodes nearby the droplet on the EWOD. This OEW mechanism can offer device simplicity by fully eliminating complex fabrication procedures (e.g., photolithography) necessary for electrode patterning, wiring, and interconnection typically faced by conventional EWOD devices. Furthermore, the minimum droplet size to be manipulated on the OEW device can be flexibly controlled by simply adjusting the size of the light pattern, instead of the electrode size physically patterned on an EWOD device.

3. Conventional OEW technologies

With the benefits of device simplicity and flexibility, OEW technologies have been developed. This chapter will discuss the fundamentals of conventional OEW devices and introduce how OEW technologies have been advanced to offer device simplicity and flexibility over EWOD devices.

3.1 Early-stage OEW devices

The concept of OEW as a light-driven droplet actuation mechanism was first introduced by Chiou *et al.*⁴⁷ Fig. 4 shows schematic illustrations of the OEW device. This early-stage OEW device was similarly structured to conventional EWOD devices where a liquid droplet is squeezed between two parallel plates. A top plate of the OEW device was composed of a hydrophobic-coated electrode, while a bottom plate was much more complicated than that of EWOD devices. The bottom plate consisted of the electrowetting (i.e., 2D arrayed) electrodes and the grid electrodes between which a photoconductive layer of amorphous silicon (a-Si) was inserted. Subsequently, silicon dioxide (SiO_2) and Teflon layers were deposited on top of the 2D arrayed electrode layer to provide dielectric and hydrophobic properties (see Fig. 4a).

To implement optical droplet actuation, an AC bias voltage was applied between the top plate and the bottom grid electrodes (Fig. 4b). As discussed in the previous section, with the absence of light illumination (i.e., a dark state), the electric impedance is dominant across the a-Si layer, where majority of the voltage drop occurs. Hence, a very small amount of the voltage drop is created across the SiO_2 layer, resulting in the negligible contact angle change with no droplet actuation.

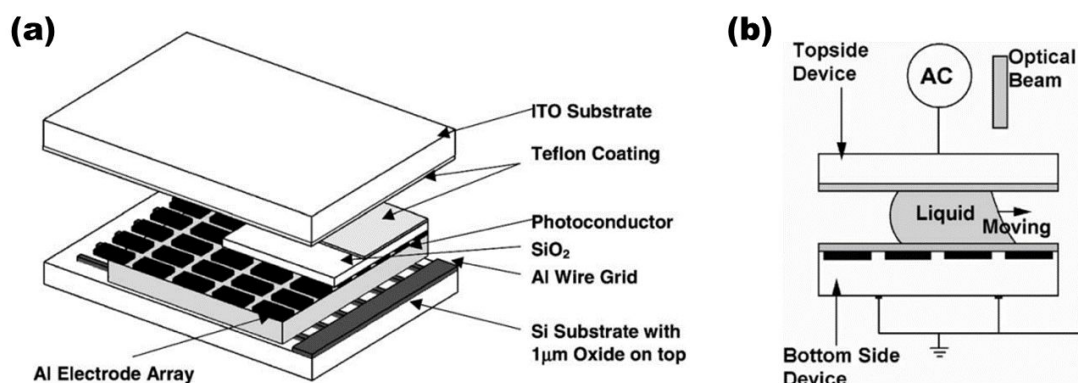


Fig. 4 An early stage optoelectrowetting (OEW) device. (a) A schematic structure of an early-stage OEW device consisting of two parallel plates. (b) Droplet actuation on the OEW device, where a liquid droplet is sandwiched between two parallel plates. Reproduced with permission from Ref. ⁴⁷

However, when an optical beam illuminates at one edge of the droplet, the conductivity of the a-Si layer significantly increases by several orders and switches most of the voltage drop across the SiO₂ layer at the light illuminated area. This caused a local electrowetting effect to form the advancing angle (θ_{adv}) of the droplet. Consequently, a pressure gradient inside the droplet gives rise to the droplet actuation towards the area the optical beam illuminates (Fig. 4b). In experiments, the transportation of a droplet (approximately 1.6 μ L) has been optically accomplished on an active device area of 1.0 \times 1.0 cm² using a 4.0 mW laser (532 nm). By applying an AC voltage at 200 V_{pp} with a frequency of 500 Hz, a droplet speed of 7.0 mm/s was demonstrated. Detailed experimental conditions and results are provided in Table 1.

Chiou *et al.* went on to further develop the OEW technology into a microfluidic system that can perform a complete set of droplet manipulation functions such as droplet

injection, transportation, merging, mixing, and splitting using a laser illumination controlled by programmable scanning mirrors.⁷⁴ Fig. 5 shows the device structure designed as a sandwiched configuration. However, this OEW device offered easy fabrication by patterning both the 2D arrayed electrowetting electrodes and the grid electrodes on the same plane of a glass substrate, unlike the previous OEW device where the layers of the electrowetting and grid electrodes were vertically separated by the photoconductive layer. Then, these electrowetting electrodes were connected to the grid electrodes via photoconductive bridges made of hydrogenated amorphous silicon (a-Si:H), followed by the layers of SiO₂ and Teflon to provide dielectric and hydrophobic properties (Fig. 5a).

The droplet actuation principle of this OEW device is like previously discussed. An AC bias voltage at 500 Hz was applied between the top and bottom grid electrodes. Under the

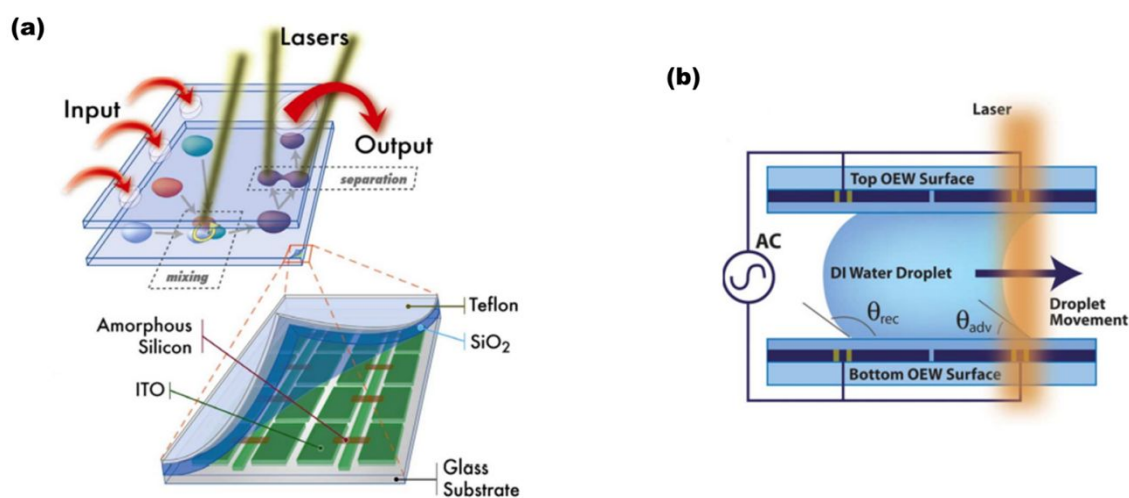


Fig. 5 An OEW-based microfluidic system. (a) The complete set of droplet manipulation functions such as droplet injection, transportation, merging, mixing, and splitting have been demonstrated using OEW technology as an active-type microfluidic system. (b) Droplet actuation on the OEW. Reproduced with permission from Ref. ⁷⁴.

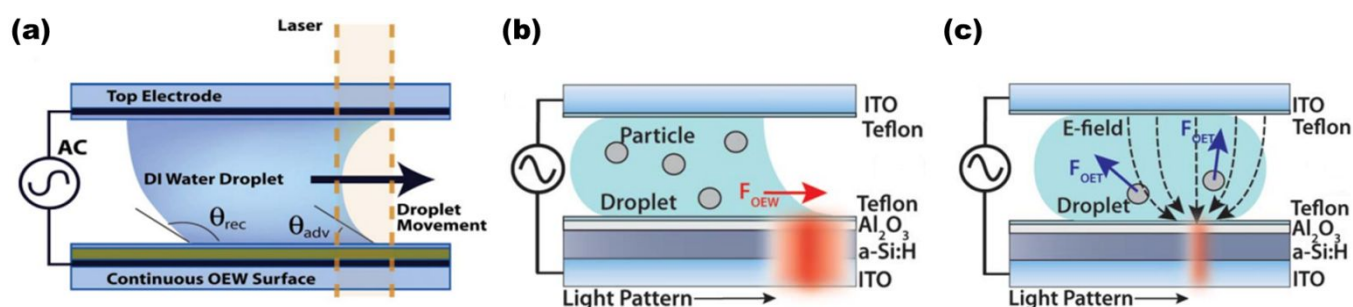


Fig. 6 Continuous optoelectrowetting (COEW). (a) A COEW device configuration can be fabricated with several featureless layers by eliminating patterning processes. When a light pattern is illuminated on a continuous photoconductive film, it creates a localized electric field concentration resulting in a net electro-mechanical force on the liquid droplet. (b) A united COEW device enables both OEW-based droplet transportation at $f = 10$ kHz and (c) dielectrophoretic (DEP) manipulation of single cells within the droplet at $f = 200$ kHz by simply adjusting the AC frequency applied at the same platform. Reproduced with permission from Ref. ^{58, 76}.

condition of no light illumination, the a-Si:H bridges would have an electrical impedance a few orders greater than that of the SiO₂ layer. As a result, the electrowetting electrodes could not be activated, and the voltage drop across the SiO₂ layer became negligible with no contact angle modification. However, when light is illuminated near one edge of the droplet, the photoconductivity of the a-Si:H bridges would significantly increase to electrically activate the nearby electrowetting electrodes at the light illuminated area (Fig. 5b). This optical addressing on the electrodes makes majority of the voltage drop across the top and bottom SiO₂ dielectric layers of the device to induce an electrowetting effect. As the droplet contact angles at both top and bottom plates decrease to form the θ_{adv} , an asymmetric droplet meniscus is created, where surface tension forces resulted in a net pressure that makes a droplet move towards the illuminated light beam. Experimentally, various droplet-based microfluidic functions, including droplet injection, transportation, splitting, multi-droplet manipulations have been successfully demonstrated on the OEW device with an active area of 1.0×1.0 cm², using a 5.0 mW laser (532 nm) as the light source. A maximum droplet actuation speed of 78 mm/s was achieved with a 0.4 μ L water droplet.

Drawbacks

By utilizing the optical method to activate the electrowetting electrodes, these early-stage OEW devices eliminated complex wiring issues typically faced by conventional EWOD devices, such as the need to individually connect large numbers of the 2D arrayed electrodes. However, since these OEW devices were similarly designed to EWOD, device fabrication was still complicated due to the photolithographic processes required for patterning of 2D arrayed electrodes and photoconductive bridges.

3.2 Continuous optoelectrowetting (COEW)

To address the fabrication issue of the early-stage OEW devices, a continuous (i.e., no patterned) optoelectrowetting (COEW)

mechanism has been proposed.⁷⁵⁻⁷⁷ It was designed as a sandwiched configuration similar to the previous OEW,^{47, 74} but with the photoconductive and electrode layers continuously deposited. As shown in Fig. 6(a), the top plate consisted of a transparent ITO electrode covered with a hydrophobic-coated dielectric layer. The bottom plate, however, provided an OEW surface made up of several featureless layers in the order of hydrophobic-coated dielectric and photoconductive on top of an electrode layer. Not only did these continuous layers fully eliminate the need for patterning processes (e.g., photolithography) to facilitate device fabrication, they also enable a droplet to be flexibly positioned at any location on the featureless photoconductive surface to allow continuous droplet transportation. The working principle of the COEW device is similar to previous OEW devices. While applying an AC bias voltage between the top and bottom electrodes, most of the input voltage drops within the a-Si layer due to its dominant electrical impedance under the condition of no light illumination. This meant that the voltage drop across the SiO₂ layer is a very small, resulting no droplet movement. To achieve droplet actuation, a light beam illuminates nearby a droplet. Thus, the photoconductivity of the a-Si layer locally increases by several orders, forming a virtual electrode due to the generation of excess electron-hole pairs at the illuminated area. This significantly reduces its electrical impedance and shifts most of the voltage drop to the SiO₂ layer. Consequently, the droplet's contact angle decreases to form an advancing angle (θ_{adv}), driving it towards the light illuminated area. Using a 0.8 mW HeNe laser (632 nm) as a light source, transportation of droplets in a picoliter volume ($10 \sim 50$ pL) have been achieved on a continuous photoconductive surface at a speed of 1.0 mm/s.

Later, Pei *et al.* improved the COEW's performance by replacing SiO₂ with aluminum oxide (Al₂O₃) as the dielectric layer deposited by an atomic layer deposition (ALD) method ⁷⁸. With the Al₂O₃ layer offering a higher dielectric constant than the SiO₂, the magnitude of the AC bias voltage applied on a COEW device could be reduced as low as 16 V_{pp}. In addition,

instead of a laser beam used in previous studies,^{47, 74} an optical projector with as much as a 85-fold lower light intensity was used to induce virtual electrodes on the OEW surface of the device. Experimentally, large-scale manipulation of liquid droplets ranging from 5 nL to 2 μ L have been demonstrated at a droplet actuation speed of 2.0 cm/s on the COEW device surface. Furthermore, Valley *et al.* have presented a unified COEW platform that enabled both OEW and dielectrophoretic (DEP) operations for on-chip manipulation of droplets as well as particles by simply altering the applied AC frequency.⁵⁸ The device performed both OEW-based droplet manipulation in the volumes ranging from 12.5 ~ 335 nL at 10 kHz (Fig. 6b) as well as dielectrophoretic (DEP) manipulation of individual cells (diameter \sim 10 μ m) inside the droplet at 200 kHz (Fig. 6c) using an optical projector ($<$ 1.0 W/cm²). Valley *et al.* have demonstrated OEW droplet actuation at a speed of up to 8.0 mm/s.

Drawbacks

Compared to early-stage OEW devices designed with 2D arrayed electrowetting electrodes and photoconductive bridges, the COEW mechanism have offered easy device fabrication with the featureless (i.e., no patterned) surface where a droplet can be positioned at any location of the device. Furthermore, the minimum droplet size governed by the size of the physically patterned electrodes typically observed in early-stage OEW devices has been fully eliminated on the continuous surface. Nevertheless, the COEW device still faces the issue of device interfacing with other microfluidic components due to its sandwiched (i.e., closed) structure. This closed device configuration seriously limited their flexibility and extensibility with integration of external microfluidic components (e.g., external reservoirs, optical detectors).

3.3 Open optoelectrowetting (o-OEW)

An open optoelectrowetting (o-OEW) configuration has been later proposed to eliminate this deficiency.^{53, 79} Unlike previously discussed OEW works, the o-OEW device has an open (i.e., single-sided) configuration, but still consisting of patterned electrodes covered with a hydrophobic-coated dielectric layer on a photoconductive (a-Si) layer. Its working principle is similar to previously discussed. With an AC bias voltage applied to the patterned electrodes, light illumination enabled to locally modify the electrical impedance in the photoconductive layer, and further dominate the voltage drop (ΔV) across the dielectric layer at the illuminated area. This light-enabled switching effect on the voltage drop makes the droplet's contact angle decrease for optical droplet actuation. Using a 3.0 mW laser (670 nm) as a light source, droplet transportation at a speed of as fast as 3.6 mm/s was achieved. More recently, Loo *et al.* developed another variation of o-OEW by integrating a conductive metal grid mesh on the OEW surface of the device.⁵¹ The device

demonstrated OEW-based dispensing and merging of 1 μ L droplets using a 1.5 W/cm² optical projector, achieving a droplet speed of 4.5 cm/s.

Drawbacks

Nevertheless, the o-OEW still shares the limitations of early-stage OEW devices. Not only are the patterning processes of 2D arrayed electrodes still required, but the minimum droplet size that can be manipulated on an o-OEW device has remained constrained by the size of the arrayed electrodes

4. Further developments in OEW

The increasing attractiveness of optoelectrowetting (OEW) has seen the technology progresses over the past few years. In this section, further developments and advances in OEW technologies will be discussed.

4.1 Single-sided continuous optoelectrowetting (SCOEW)

To overcome the main issues highlighted by all previous OEW studies,^{47, 53, 58, 74-79} Park *et al.* have developed a new OEW mechanism, called single-sided continuous optoelectrowetting (SCOEW).⁸⁰ This SCOEW mechanism combines the benefits from both the COEW and o-OEW devices. It has a single-sided (i.e., open) configuration that ensures a flexible interface for easy integration with other external microfluidic components (e.g., optical detectors, reagent reservoirs, microchannel devices, etc.) and easy accessibility to reagent droplets placed on an open surface. At the same time, a continuous and featureless configuration offers device simplicity in fabrication as well as high versatility and extensibility by eliminating the limitation of the minimum droplet size and allowing droplets to be continuously positioned at any location on a 2D planar surface. More importantly, unlike all previous OEW devices, the operation of the SCOEW mechanism is based on a lateral field modulation. This SCOEW mechanism allows the use of low-intensity light sources such as an LCD display (as much as 4 orders lower intensity than lasers or optical projectors commonly used in previous OEW studies) without any additional optical components such as lenses. These unique aspects of the SCOEW will be detailed in following sections.

Fig. 7 shows schematic illustrations of the SCOEW device in a single-sided continuous configuration. The device fabrication begins with the deposition of a photoconductive (a-Si:H) layer on a glass substrate using plasma enhanced chemical vapor deposition (PECVD). On top of the a-Si:H layer, only two aluminum (Al) electrodes are required to be patterned at both edges of the device. Then, an amorphous fluorocarbon polymer, called Cytop, was spun coated to provide hydrophobic and dielectric properties. Compared to previous OEW devices, the continuous configuration of the SCOEW offers simple device

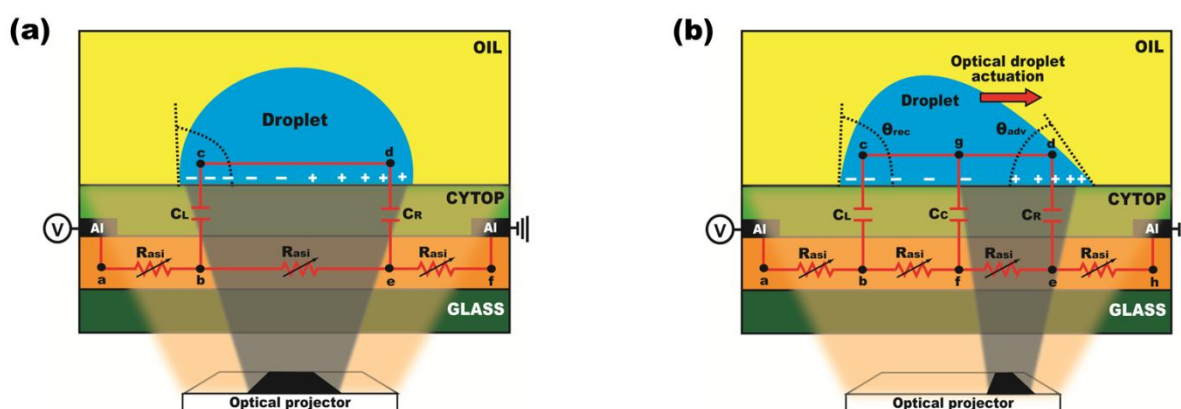


Fig. 7 Single-sided continuous optoelectrowetting (SCOEW). A schematic of the SCOEW device is shown with its equivalent circuit model. (a) When a dark pattern symmetrically illuminates in the middle of the droplet, the photo-resistance increases at the area illuminated by the dark pattern. However, ΔV across the capacitors at both edges of the droplet increases by the same magnitude such that $\Delta V_{bc} = \Delta V_{de}$ which corresponds to the droplet spreading out symmetrically to have its contact angle of θ . (b) When a dark pattern illuminates onto one side of the droplet, the photo-resistance asymmetrically increases, causing a voltage drop difference at droplet edges (i.e. $\Delta V_{bc} > \Delta V_{de}$). As the contact angle decreases to form an advancing angle, θ_{adv} , the asymmetric droplet shape creates a pressure gradient inside the droplet that actuates it in the direction of the dark pattern. Reproduced with permission from Ref.⁸⁰.

fabrication without any photolithographic processes for patterning and wiring of 2D arrayed electrowetting electrodes.

A droplet actuation principle on the SCOEW can be qualitatively explained using an equivalent circuit model presented in Fig. 7. Unlike previous OEW mechanisms, the SCOEW utilizes a direct current (DC) bias voltage applied between the two electrodes positioned at edges of the device. Thus, a uniform electric field is generated along the lateral direction to form a shunt circuit, where the photoconductive layer can be equivalently modeled as photoresistors in a series connection and the dielectric layer is equivalent to have capacitors in a parallel connection. Since the electric conductivity of the liquid droplet is much higher as compared to the other layers, its electrical impedance can be neglected. Under the uniform electric field distributed along a lateral direction, a droplet remains almost symmetrically with its initial contact angle θ_0 in an oil medium, resulting no droplet actuation. When a dark pattern is illuminated in the middle of the droplet (Fig. 7a), the photo-resistance of the a-Si:H increases only at the area (between the nodes *b* and *e*) illuminated by a dark pattern, and the voltage drop (i.e., ΔV_{be}) correspondingly increases as well. However, this voltage drop can be equally divided into across two capacitors of c_L and c_R at the edges of the droplet (i.e., $\Delta V_{bc} = \Delta V_{de} = 1/2\Delta V_{be}$). These equal voltage drops maintain the droplet symmetrically with the same contact angles on both sides, leading to no droplet movement. However, in the case of asymmetric illumination, where a dark pattern is projected onto one side of the droplet (Fig. 7b), the photo-resistance of the a-Si:H layer increases at the dark illuminated area, resulting in an asymmetrical increase in the voltage drop at the corresponding side of the droplet (i.e., $\Delta V_{bc} \neq \Delta V_{de}$). This leads to the formation of the advancing (θ_{adv}) and receding (θ_{rec}) contact angles to actuate the droplet towards the direction of the dark pattern illuminated.

When compared to prior OEW studies,^{47, 53, 58, 74-79} the SCOEW mechanism provides an important and unique feature for droplet actuation. Due to the formation of a shunt equivalent circuit composed of the dielectric capacitors and the photoresistors (see Fig. 7), the electrowetting voltages across the two capacitors of c_L and c_R are determined by the relative ratio of photo-resistances between the nodes *b* and *e*, not by their absolute values. Therefore, even a 2-fold ratio in the photoconductivity between the illuminated and non-illuminated sites, i.e., $b = 2$, is sufficient to induce droplet actuation. This unique characteristic allows optical actuation of droplets with a low optical intensity for large area manipulations on a SCOEW device. With this interesting characteristic, later SCOEW studies have demonstrated the use of a smartphone as a low-intensity light source and the use of a polymer-based low-quality photoconductive material to offer cost-effective, portable, lab-on-a-chip (LOC) platforms.^{50, 55, 56}

Numerical simulation studies

The droplet actuation principle mentioned above for the SCOEW has been validated by 3D simulation works implemented using COMSOL Multiphysics.⁸⁰ For the simulation studies, a hemispherical water droplet was modelled to be positioned on the device composed of 10 μm dielectric, 5 μm photoconductive, and 550 μm thick electrically insulating-dielectric oil layers. With a DC bias voltage at 100 V is applied at both end planes separated by a 1.0 mm gap to provide a uniform electric field along a lateral direction. To represent a low-quality photoconductive property, the electric conductivity of the photoconductive layer was assumed as $\sigma_{\text{photo}} = 2 \times 10^{-8}$ S/m at a photo state and $\sigma_{\text{dark}} = 1 \times 10^{-8}$ S/m at a dark state with an only 2-fold ratio (i.e., $b = 2$). Fig. 8 presents the simulation results of the electric field distribution as the top and side views, and voltage profiles under: (a) a symmetric illumination of a

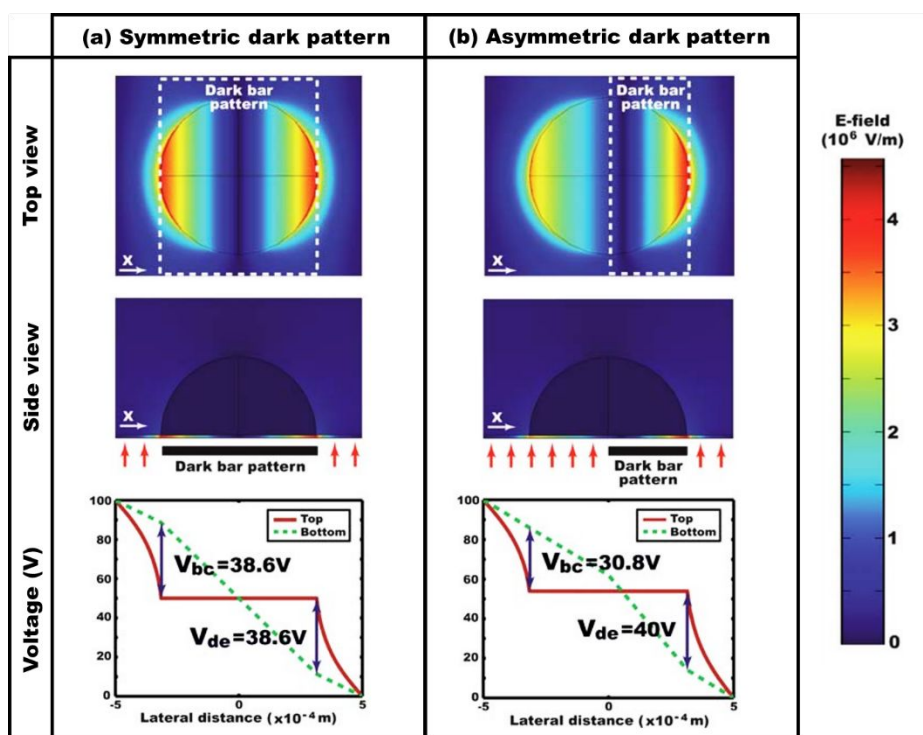


Fig. 8 3D numerical simulation results showing electric field distribution and voltage profiles under various dark pattern illuminations. (a) When a dark pattern as wide as the base diameter of the droplet is symmetrically projected in the middle of the droplet, the voltage drops are equal on both droplet edges ($\Delta V_{bc} = \Delta V_{de} = 38.6$ V) as the droplet spreads out symmetrically to have a contact angle of 90° with no droplet actuation. (b) When a dark pattern half the size of the droplet asymmetrically illuminates on one side of the droplet, the resistance of the a-Si-H layer asymmetrically increases at the only area a dark pattern illuminates. As a result, the voltage drops at the droplet edges are differently created (i.e., $\Delta V_{bc} = 30.8$ V $<$ $\Delta V_{de} = 40.0$ V), causing the advancing (θ_{adv}) and receding (θ_{rec}) angles to optically drive the droplet towards the dark pattern projected. Reproduced with permission from Ref.⁸⁰.

dark pattern, and (b) an asymmetric illumination of a dark pattern. The voltage distribution profiles extracted from the top (solid lines) and bottom (dotted lines) surface of the dielectric layer are depicted. The voltage differences between these top and bottom surfaces of the dielectric layer indicates the voltage drop, ΔV_{bc} and ΔV_{de} , at the left and the right edge of the droplet, which determines the advancing (θ_{adv}) and receding (θ_{rec}) angles of the droplet as estimated by the Young-Lippmann Eq. (1). In Fig. 8(a), when a dark-bar shaped pattern is symmetrically projected in the middle of the droplet, a 2-fold photo-resistance increases only at the area where a dark pattern illuminates. However, no droplet actuation can be achieved due to the equal voltage drops (i.e., $\Delta V_{bc} = \Delta V_{de} = 38.6$ V) at both edges of the droplet. On the other hand, in Fig. 8(b), a dark pattern asymmetrically projected to one side of the droplet causes an increase in the photo-resistance only at the area illuminated by the dark pattern. As a result, the droplet undergoes the unbalanced voltage drop (i.e., $\Delta V_{bc} = 30.8$ V $<$ $\Delta V_{de} = 40.0$ V) at its edges, causing the advancing (θ_{adv}) and receding (θ_{rec}) angles to optically drive the droplet towards the dark pattern projected. This simulation study has verified the droplet actuation principle of the SCOEW that is based on relative voltage control, as discussed in Fig. 7.

Experimental demonstrations

Fig. 9(a) and (b) depict continuous light-actuated droplet transportation on a SCOEW device using a commercially available optical projector as a light source to provide dynamic light patterns. Interestingly, by simply adjusting the size of a dark pattern, droplet transportation could be achieved in a wide range of the droplet volumes from 50 μ L (Fig. 9a) to 250 μ L (Fig. 9b) on the same SCOEW device without any extra optical components (i.e., lenses for light focusing). To further demonstrate the requirement of a low-intensity light source, Fig. 9(c) shows the device being gently placed on an LCD computer monitor that provides the 4 orders lower light intensity than that of lasers or optical projectors commonly used for previous OEW studies. With a 1.3 mm wide dark pattern directly illuminated from an LCD monitor with any extra lens, a 0.5 μ L water droplet could be optically transported by at a speed of 510 mm/s. Various other droplet manipulation functions were demonstrated as well. Fig. 9(d) presents the splitting of a 1 μ L droplet by the sudden illumination of a 6 mm wide dark pattern. In Fig. 9(e), two water droplets, one 0.5 μ L (dissolved with a green dye) and one 2 μ L, experienced electrocoalescence for merging due to the dipole-dipole interaction between the two droplets. To mix the contents in the combined droplet, the droplet was optically driven across the SCOEW device surface by a moving dark pattern. This process created a shear force from the bottom, which caused an internal flow to induce droplet mixing.

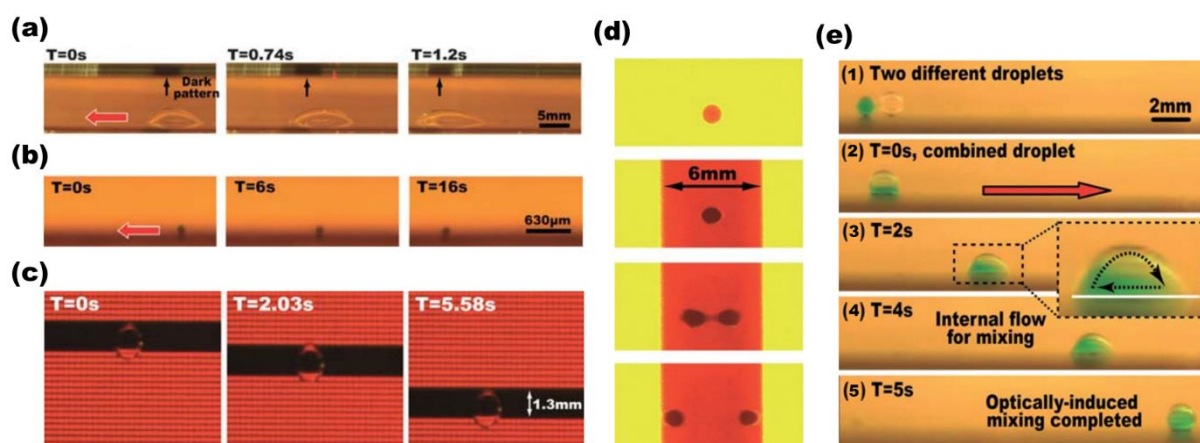


Fig. 9 Various light-driven droplet manipulations with the SCOEW. Experimental demonstrations of continuous transportations of a water droplet in a volume of (a) 50 μL and (b) 250 μL by simply adjusting the size of a dark pattern. (c) To realize the requirement of a low-intensity light source, actuation of a 0.5 μL droplet on an LCD display was conducted. Other droplet manipulation functions such as (d) splitting of a 1 μL droplet and (e) merging and mixing of two droplets (0.5 μL and 2 μL) were also demonstrated. Reproduced with permission from Ref. ⁸⁰.

The SCOEW's capability for integration with other microfluidic components on a single-sided surface has also been demonstrated. For example, the schematic illustration in Fig. 10(a) depicts an external sample reservoir being integrated with a SCOEW device through a pin connector. With dynamic optical patterns being programmed onto the SCOEW device, droplet injection can be triggered from the sample reservoir. Fig. 10(b) shows video snapshots of the light-triggered droplet injection, where 2.5 μL water droplets were being continuously injected from the sample reservoir into a SCOEW chamber at a constant speed of 1 mm/s. To highlight precise droplet volume dispensing on the SCOEW, digital images of the injected droplets were analyzed with an image processing toolbox (using MATLAB). As indicated in Fig. 10(c), it was examined that there was less than 1% in volume variation between the injected droplets. Further demonstrations on parallel light-triggered

droplet injection were presented in Fig. 10(d). Using two dark bar conveyors moving at the speed but with different periodicities, 1.8 μL (top conveyor) and 0.9 μL droplets (bottom conveyor) were continuously injected from two separate reservoirs and successfully transported along the SCOEW surface.

Later, Shekar *et al.* developed another SCOEW device using a 25 nm thin Al_2O_3 layer as a dielectric.⁵² This dielectric layer helped to increase the effective capacitance of the dielectric region, thereby reducing the required threshold voltage for droplet manipulation by as much as 2 orders. The device was patterned with multiple electrodes for multi-directional droplet manipulations. By using a 1.5 W/cm^2 optical projector with a lateral electric field of 24 V/cm , a maximum transportation speed of 12 mm/s can be achieved with a 20 μL droplet. More recently, Liu *et al.* demonstrated

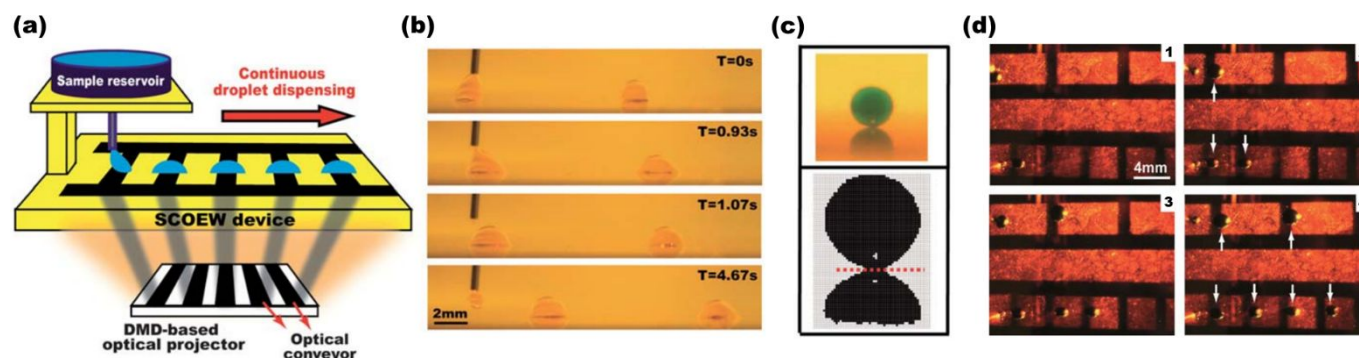


Fig. 10 The SCOEW's capability for flexible integration with other microfluidic components. (a) A schematic drawing of an external sample reservoir being integrated with the SCOEW for light-triggered droplet injection. (b) 2.5 μL droplets being continuously injected from the sample reservoir into a SCOEW chamber. (c) Image analysis of the injected droplets with less than 1% in volume variation, demonstrating precise volume control of the SCOEW. (d) Experimental demonstrations of parallel light-triggered droplet injection from two external reservoirs, where 1.8 μL (top conveyor) and 0.9 μL droplets (bottom conveyor) were continuously injected and transported along the SCOEW surface with different periodicities. Reproduced with permission from Ref. ⁸⁰.

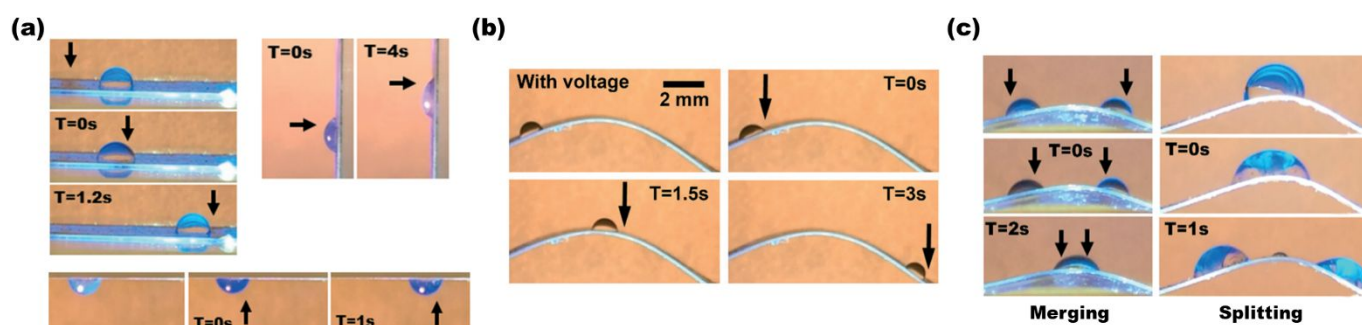


Fig. 11 Light-driven 3D droplet manipulations with flexible SCOEW technology. (a) Experimental demonstrations of droplet transportations on various 3D terrains such as flat, vertical, and upside-down surfaces. (b) 3D droplet transportation was also achieved on a curved surface. (c) Droplet-based functions of merging and splitting on a curved surface are also demonstrated. Black arrows indicate locations of the projected dark patterns. Reproduced with permission from Ref. ⁵⁰.

multidimensional droplet manipulation along arbitrary directions on a SCOEW device by projecting Z-shaped optical patterns.⁸¹ In experiments with an applied electric field of 80 V/cm (in the *x*-direction), an 8 μ L droplet can be transported in the *y*-direction (perpendicular to the direction of the electric field) at a maximum speed of 4.86 mm/s.

4.2 Flexible SCOEW device for 3D droplet manipulation

With technological advances in EWOD over the past few years, research attentions have been further extended to three-dimensional (3D) spatial control of droplets on a non-planar EWOD surface. Not only can this 3D EWOD technology allow larger volumetric capacities but also provide much more flexibility and functionality than two-dimensional (2D) planar devices. Relevant studies to 3D EWOD technology have been widely demonstrated, including droplet actuation on uneven terrains,⁸²⁻⁸⁴ vertical translation,⁸⁵⁻⁸⁸ droplet jumping,⁸⁹⁻⁹² even in the form of wearable wristbands for portable point-of-care (POC) applications,^{93, 94} and new fabrication methods of 3D devices.⁹⁵⁻⁹⁷ Despite such numerous works on 3D EWOD technology, it was challenging for OEW researchers to demonstrate light-driven 3D droplet manipulations on flexible substrates due to the incompatibility of depositing photoconductive materials that have been commonly used for previous OEW devices onto flexible substrates. Park's group has recently presented a flexible SCOEW technology to overcome this critical issue by utilizing a polymer-based photoconductive material.⁵⁰

As discussed earlier, all previous OEW studies have used the *a*-Si material to provide a photoconductive property.^{47, 53, 58, 74-80} However, an issue associated with the *a*-Si is the requirement of conventional integrated circuit (IC) processes such as chemical vapor deposition (CVD) or plasma enhanced chemical vapor deposition (PECVD) for its thin-film layer deposition.⁹⁸⁻¹⁰⁰ These IC fabrication processes typically require complex and expensive laboratory setups like high vacuum facilities and have to be operated at high temperatures of over 300 °C.^{100, 101} Nevertheless, most of the commercially available

flexible substrates such as polyethylene terephthalate (PET) and polyethylene naphthalate (PEN) detrimentally experience thermal deformation under such high-temperature conditions over 300 °C.^{102, 103} This compatibility issue has seriously prevented OEW devices from being fabricated on flexible substrates for 3D droplet applications. Jiang *et al.* overcame such a compatibility issue by substituting the *a*-Si material with titanium oxide phthalocyanine (TiOPc), which is a polymer-based photoconductive material.⁵⁰ The use of the TiOPc as a photoconductive material has enabled simple device fabrication on a flexible substrate via a low-cost, spin-coating method, thereby fully eliminating the need for complex and expensive high-temperature processes such as CVD or PECVD. The concept of the flexible SCOEW technology has been experimentally demonstrated, as presented in Fig. 11. In Fig. 11(a), liquid droplets were optically manipulated on various types of 3D terrains, including a flat surface (an inclined angle, $\varphi = 0^\circ$), a vertical surface ($\varphi = 90^\circ$), as well as an upside-down surface ($\varphi = 180^\circ$). 3D droplet transportation on a curved surface was experimentally demonstrated in Fig. 11(b). In addition, the SCOEW's capabilities for droplet merging and splitting have been further demonstrated on a 3D curved surface (Fig. 11c).

Previous OEW studies have typically focused on experimental demonstrations of droplet actuation in the various device configurations, while Jiang *et al.* have interestingly discussed about analytical studies to estimate the light-induced EWOD force.⁵⁰ This analytical prediction helped us to understand an optimum size of the dark pattern relative to the droplet size at a given value of *b* (i.e., a photoconductivity ratio) to maximize an OEW force. With the small values of *b* less than 10, which represents low-quality photoconductive materials or low-intensity light illumination, the OEW force can be peaked by a dark pattern in a half size of the droplet size. As the value *b* increases, the force sharply raises up even at a small pattern size. This is because the small dark pattern is sufficient in creating a large voltage drop to maximize the OEW force due to the large conductivity change between photo and dark states,

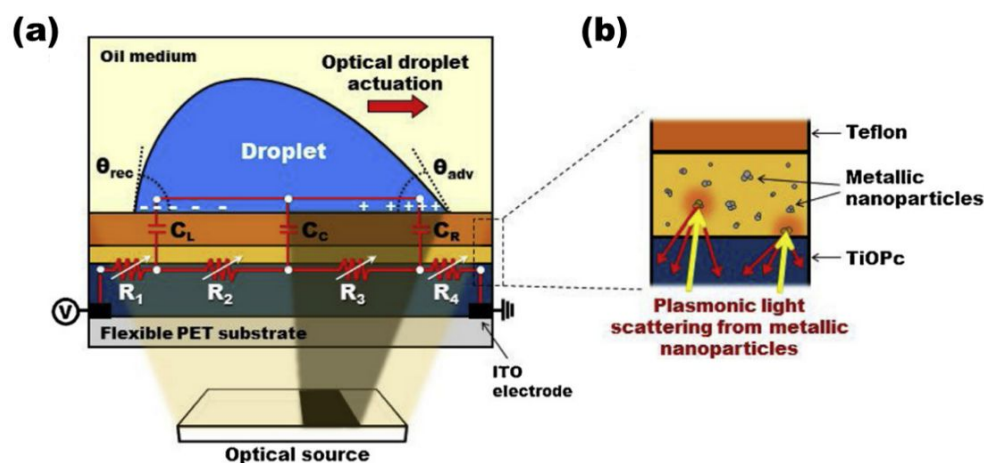


Fig. 12 Plasmonic-enhance SCOEW technology. (a) Plasmonic nanoparticles are used to improve light absorption in the photoconductive layer of a SCOEW device. (b) With the presence of a nanoparticle layer, light that are not absorbed by the TiOPc active layer will undergo plasmonic light scattering. As a result, their optical path lengths increase over a wide angular spread as more light rays are redirected back onto the TiOPc layer, enhancing light absorption and OEW performance. Reproduced with permission from Ref. ¹⁰⁷.

when the b value is high. For example, when $b = 10^3$, representing high-quality photoconductive materials or high-intensity light illumination, the OEW force is estimated as high as $45 \mu\text{N}$ (>11-fold larger compared to when $b = 5$) by projecting the dark pattern as wide as a tenth of the droplet size.

Drawbacks

With the use of the TiOPc as a photoconductive material, the flexible SCOEW technology can offer several benefits over previous OEW devices, such as low-cost and simple device fabrication, device flexibility and functionality through 3D spatial droplet manipulations on non-planar terrains. However, it has one critical drawback with regards to its low-quality photoconductive property. As reported in previous OEW studies,^{47, 50} the photoconductive performance of the TiOPc is not as significant as the a-Si. In the other word, the b value of the a-Si is in the magnitude of a few orders, whereas that of the TiOPc is in the range of a few folds. This poor photoconductive property of the TiOPc material is caused by its limited charge carrier mobility and low exciton diffusion length at the donor/acceptor interface.^{104, 105} To facilitate charge transport, a thin layer of TiOPc is required. However, a thin TiOPc layer will result in insufficient light absorption.¹⁰⁶ This greatly reduces the effect of optical activation on the OEW device, which results in a much smaller OEW force induced as compared to high-quality photoconductors like the a-Si. Hence, OEW devices would not be able to operate effectively as droplet manipulation tools. This limitation in light absorption associated with the TiOPc has been later overcome by utilizing plasmonic nanoparticles, which will be detailed in the next section.

4.3 Plasmonic-enhanced SCOEW

Thio *et al.* have developed a plasmonic-enhanced SCOEW technology to offer significant improvements in light absorption of the TiOPc by using metal nanoparticles.¹⁰⁷ For this study, the

device was fabricated to have metal nanoparticles randomly dispersed on top of the TiOPc layer via a spin-coating method before deposition of a hydrophobic-coated dielectric layer, as illustrated in Fig. 12. With the presence of nanoparticles, light rays that have been transmitted (i.e., did not get absorbed) through the TiOPc active layer will undergo plasmonic light scattering, which effectively increases their optical path length over a wide angular spread within the TiOPc layer. Thus, more light rays can be redirected back onto the TiOPc layer and result in a significantly enhanced light absorption to improve a photo-state conductivity of the TiOPc. On the other hand, the dark-state conductivity of the TiOPc at the dark illuminated area remains unchanged. This enhanced conductivity switching performance ($b = \sigma_{\text{photo}} / \sigma_{\text{dark}}$) of the TiOPc can enlarge OEW performance with much larger forces.

Several numerical simulation studies have supported the phenomenon of plasmonic light scattering and redirection back onto the TiOPc layer by adding a layer of conductive nanoparticles. Fig. 13(a) presents how the optical path lengths of incoming light rays have been increased after being scattered by a single metallic nanoparticle (50 nm in a diameter) over a wide angular spread. The scattered light intensity of each ray matches well with the Rayleigh theory, which attributes light absorption of a nanoparticle to its angular dependence on plasmonic light scattering.^{108, 109} From another simulation study, Fig. 13(b) and (c) depict a total of 20 000 input light rays being illuminated onto an array of uniformly distributed conductive nanoparticles in 3 staggered layers. Results have shown that only 22.05% of the input power emerged out from the top of the nanoparticle array as transmitted rays (Fig. 13d), while 69.95% of the input power were detected from the bottom as scattered rays. The remaining 8% of the input power were accounted by the power lost due to the angular-dependent light absorption properties by the nanoparticles (as described in Fig. 13a) as well as the continued propagation of rays within the

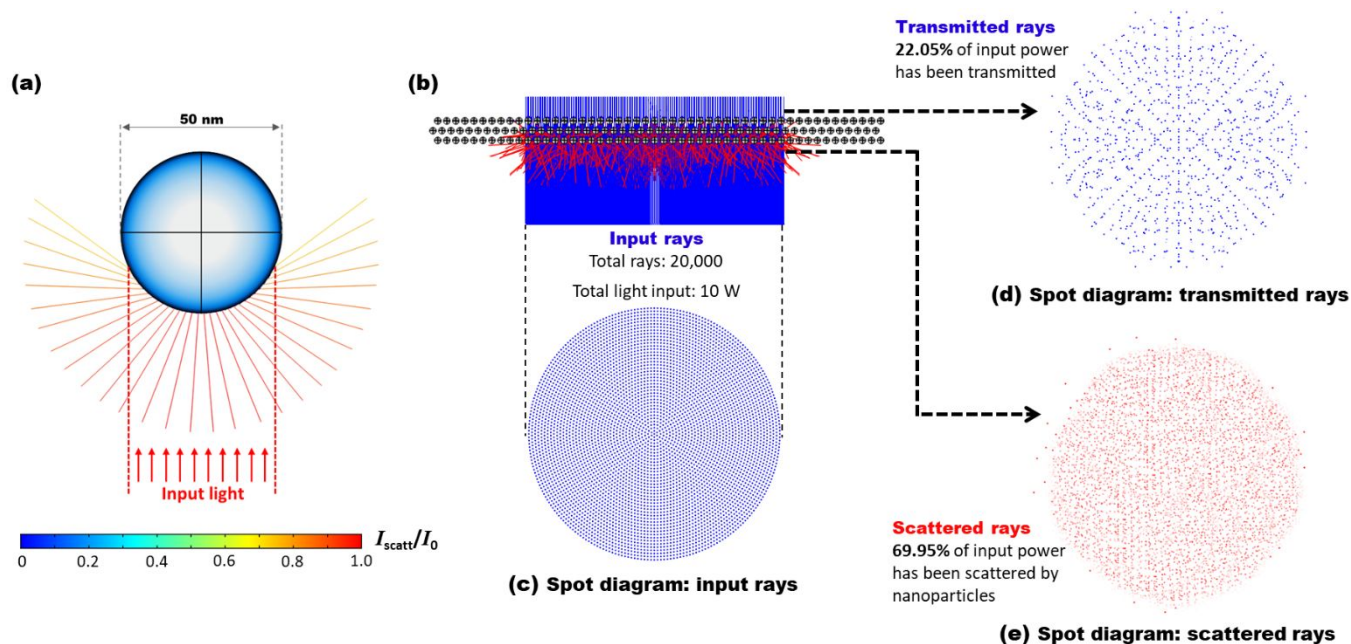


Fig. 13 Simulation results of plasmonic light scattering. (a) Input rays increase their optical path lengths after being scattered by a single nanoparticle over a wide angular spread. The angular dependence of a scattered ray intensity means that a lower scattered intensity (I_{scatt}) as compared to the input ray (I_0) is obtained at a larger direction of scatter. (b) and (c) A total of 20 000 input light rays is projected onto an array (3 staggered layers) of uniformly distributed conductive nanoparticles. (d) Only 22.05% of the input power emerged from the top as transmitted rays, while (e) 69.95% of the input power the emerged from the bottom as scattered rays. The use of nanoparticles above the low-quality TiOPc photoconductive layer in an OEW device encourages plasmonic light scattering to redirect more light rays onto the TiOPc layer, greatly improving its light absorption and photo-state conductivity. Reproduced with permission from Ref. ¹¹⁰.

nanoparticle arrays. These simulation studies demonstrated how input rays are angularly scattered by the nanoparticle before being redirected back onto the TiOPc layer to additionally contribute to the layer's light absorption and photo-state conductivity.

The plasmonic-enhanced OEW performance was also experimentally demonstrated. In Fig. 14(a), a spectrophotometric absorbance study indicated the dramatic enhancement in light absorption of the TiOPc layer with the use of thicker layers of Al nanoparticles (at 2 wt% concentration).

Another study on a droplet's static contact angle verified that an increasingly larger contact angle modulation can be attained with higher nanoparticle concentrations, showing as much as 58.9° (i.e., $\Delta\theta = 126.7^\circ - 65.8^\circ$) more contact angle modulation than the case without nanoparticles (Fig. 14b). These two experimental studies demonstrated that the thicker or denser layer of the nanoparticles, the more optical absorption onto the TiOPc layer and the more contribution to an electrowetting effect. Lastly, a light-driven droplet dynamics study in Fig. 14(c) recorded a droplet instantaneous speed as high as 12.5 mm/s

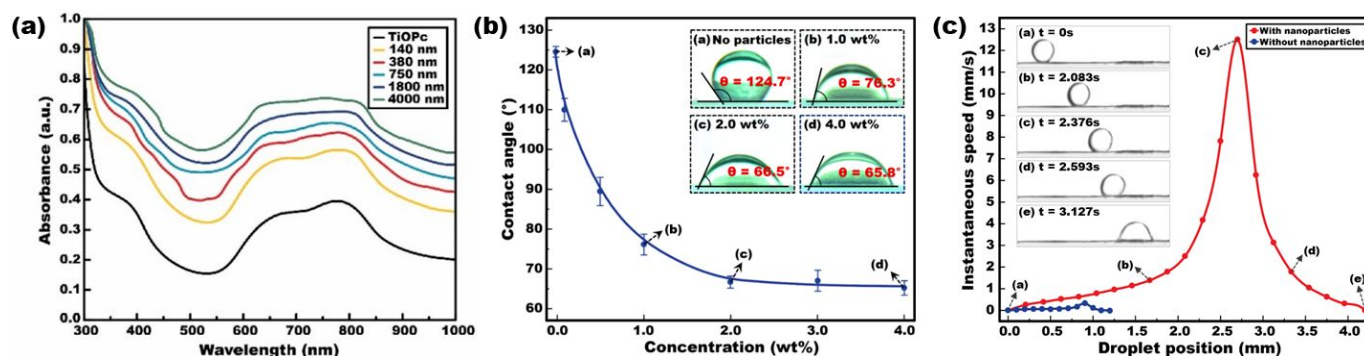


Fig. 14 Experimental demonstrations for plasmonic-enhanced SCOEW. (a) Spectrometric absorbance of a TiOPc layer when 2.0 wt% Al nanoparticles are randomly dispersed at various thicknesses. Light absorption has been greatly enhanced because of plasmonic light scattering from the nanoparticles. (b) Measurements of a droplet's static contact angle indicating that a larger contact angle modulation can be attained with higher nanoparticle concentrations. (c) Light-driven droplet dynamics demonstrating a droplet speed as high as 12.5 mm/s due to the presence of nanoparticles, which is 39 times faster than the case without the use of nanoparticles. Reproduced with permission from Ref. ¹⁰⁷.

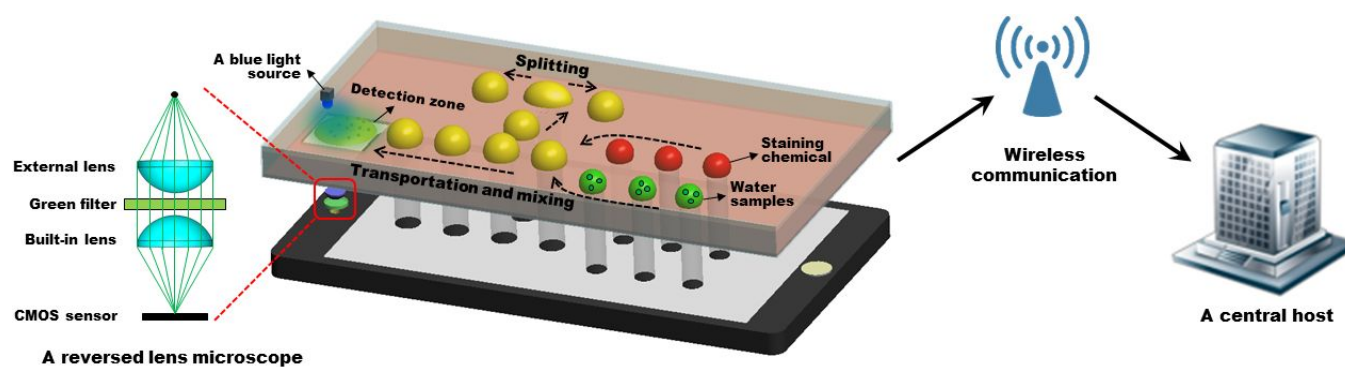


Fig. 15 The smartphone integrated optoelectrowetting platform (SiOEW). The SiOEW platform is able to perform on-chip water sample preparation and on-site monitoring of water quality. The smartphone is used to project low-intensity light patterns onto a SCOEW device for OEW-based droplet manipulation. At the same time, the smartphone allows on-chip fluorescent microscope for the detection of target algae cells in water samples by mounting several optical components above its built-in camera to form a reversed lens microscope. Finally, the smartphone can rapidly share its location and the captured data with a central host (e.g., an environmental agency). Reproduced with permission from Ref. ⁵⁶.

with the presence of nanoparticles, which is 39 times faster than the case without any use of nanoparticles.

The plasmonic-enhanced OEW technology utilizes conductive nanoparticles to induce plasmonic light scattering onto the TiOPc layer, thereby enlarging its light absorption and photo-state conductivity. This technology provides a significantly improved OEW performance for effective light-driven droplet manipulation even with a poor-quality TiOPc layer, thus offering cost effectiveness of devices in numerous potential droplet microfluidic applications.

5. OEW applications as portable smartphone-integrated environmental sensors

Water is the most essential resource for all living forms on Earth. There are various species in water systems even including viruses and bacteria. Timely detection of any hazards (e.g., toxic dinoflagellates, *Vibrio* spp., etc.) existing in water systems as well as rapid communication of relevant information with a central host are very important to properly manage water quality without contamination and pollution of water systems.^{111, 112} However, conventional methods are inefficient, costly, and labor-intensive, requiring large volumes of water samples and time-consuming laboratory-level examinations for water quality detection.¹¹³⁻¹¹⁵ To address these issues, several smartphone-integrated SCOEW studies have been proposed. In this section, the emergence of OEW technology as smartphone-integrated portable biosensors will be introduced for environmental applications.

5.1 A smartphone-based fluorescent microscope for real-time and on-site detection of harmful algae cells

With the SCOEW's benefits of device simplicity, cost effectiveness, versatility, and flexibility, Jiang *et al.* developed a smartphone-integrated optoelectrowetting (SiOEW) device to offer a portable method that is low-cost and simple for on-site

water quality detection.⁵⁶ Fig. 15 shows a schematic of the SiOEW platform to work as a portable fluorescence microscope for on-site detection of target cells in environmental water. A commercially available smartphone, which is placed below the SCOEW device, was being utilized as a low-intensity portable light source (a few orders lower intensity than lasers and optical projectors used for previous OEW studies) to illuminate dynamic optical patterns onto a photoconductive surface of the device. Using the OEW principle, various droplet-based microfluidic functions (e.g., transportation, mixing, and immobilization on a hydrophobic-coated detection zone) were carried out for on-chip processing of water samples.

To equip the SiOEW with the capability for on-chip fluorescence microscopic detection of the target algae cells in water samples, a reversed smartphone lens microscope was developed using two identical smartphone lens modules and a green bandpass filter inserted between the lens modules.¹¹⁶ This reversed lens microscope has ensured a full coverage of the smartphone's complementary metal-oxide-semiconductor (CMOS) sensor due to the perfectly matched angular field of views of the identical lens modules. With the presence of a blue LED light bulb for fluorescent excitation, the only stained target cells in water samples are detected by a smartphone's built-in digital camera after passing through the reversed lens microscope that allows up to 45 \times magnification for on-chip water quality analyses. Additionally, the smartphone is equipped with various functions such as wireless communications and global positioning system (GPS) capability. These capabilities allow captured data (e.g., location tracking, time of test conducted) to be shared instantly and wirelessly with a central host (e.g., an environmental regulation agency) for real-time monitoring and management of water quality.

To further improve device portability for on-site water quality detection, Lee *et al.* developed a 3D-printed hand-held SiOEW platform, where various optical and electrical components such as smartphone, external lens module, voltage

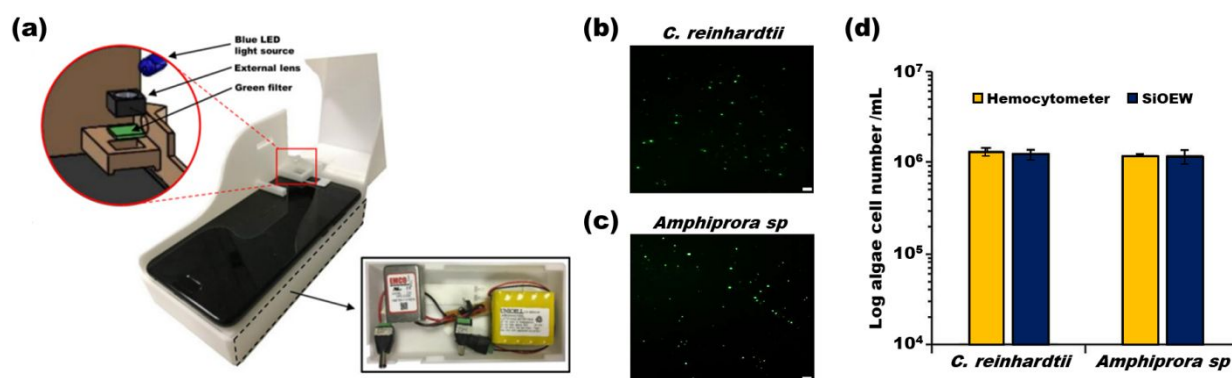


Fig. 16 An automated 3D-printed SiOEW platform. (a) A 3D-printed platform housing all the optical and electrical components together to enhance device portability. These components include a smartphone, SCOEW device, lens module, and voltage source. On-chip fluorescent microscopic detection and digital images of harmful algae cells in (b) freshwater sample spiked with *C. reinhardtii* and (c) marine water sample spiked with *Amphiprora* sp. captured by an integrated smartphone. (d) Cell counting comparison between a regular microscopy method using a hemocytometer and the SiOEW approach, showing cell populations in the same orders. Reproduced with permission from Ref. ¹¹⁷.

source and a SCOEW device were compactly assembled together (see Fig. 16a).^{117, 118} This hand-held SiOEW platform is capable of performing on-chip water sample preparation as well as rapid and in-situ monitoring of viable algae in water samples directly collected from local reservoirs and coastline. For experimental demonstrations of on-chip fluorescent microscopic detection, Fig. 16(b) and (c) present the digital images of harmful algae cells in freshwater sample spiked with *C. reinhardtii* and marine water sample spiked with *Amphiprora* sp. that were captured by a smartphone's digital camera. A smartphone app was further used to count the populations of the harmful algae cells in water samples. In Fig. 16(d), a cell counting comparison between a regular microscopy method (i.e., using a hemocytometer) and the SiOEW approach was presented. The measured cell population data show that the 3D-printed SiOEW platform can provide comparable results for the target cell counting in the same orders as the hemocytometer.

5.2 A lab-on-a-smartphone (LOS) platform for on-site detection of fecal contamination in water via LAMP assay

Being able to provide rapid and on-site detection of waterborne pathogens in environmental waters essentially safeguards the public health from the dangers of fecal contamination. In recent years, Thio *et al.* developed another smartphone-integrated SCOEW platform, called a lab-on-a-smartphone (LOS), as a portable, low-cost, and fully integrated system that enables rapid, in-situ monitoring of fecal indicator bacteria (FIB) and their associated pathogens in environmental water without the need for sophisticated laboratory equipment or skilled personnel.⁵⁵ The LOS was developed as a portable platform where three main components, a plasmonic-enhanced OEW device, a transparent heater, and a commercially available smartphone, are compactly integrated to eliminate the need of auxiliary optical and mechanical components (e.g., pumps and

tubes to feed individual reagents, microscope and CCD camera for microscopic analyses) typically required for a conventional lab-on-a-chip (LOC) setup. As shown in Fig. 17(a) and (b), a plasmonic-enhanced OEW device performs pumpless and tubeless droplet manipulations for on-chip water sample preparations of fecal indicator bacteria (FIB) and corresponding LAMP mixture in an oil chamber. Secondly, the integration of a transparent heater to the bottom surface of the plasmonic-enhanced OEW device equips the LOS platform with the capability to conveniently perform LAMP assays for in-situ analysis of water quality. This enabled on-chip isothermal nucleic acid amplification at 65 °C without bulky and expensive equipment like a thermal cycler (Fig. 17c). Lastly, various features on the integrated smartphone can eliminate the need for auxiliary equipment and components. For example, a smartphone's display screen serves as a low-intensity light source to project dynamic light patterns onto a photoconductive surface of the plasmonic-enhanced OEW device for effective optical manipulation of oil-immersed water samples. Due to the single-sided, open-chamber configuration of the LOS, the smartphone can also be easily integrated as a portable optical detector to conveniently implement on-chip molecular detection of FIB (Fig. 17d). For a real-time colorimetric assessment of the LAMP assay results, the smartphone's built-in camera was first used to capture digital images of the target water samples. Next, its image processing app was further used for quantitative analysis of time-dependent color changes of the target samples by computing their red-green-blue (RGB) values.

Fig. 18(a) shows an experimental demonstration of on-chip *E. coli* sample processing on a plasmonic-enhanced OEW device, where two droplets of 1.0 μ L freshwater spiked with *E. coli* DNA and a 1.5 μ L LAMP mixture were successfully merged, transported, and mixed when dynamic optical patterns were projected from a smartphone placed below. Fig. 18(b) presents the digital images of the droplet taken at 10 min intervals

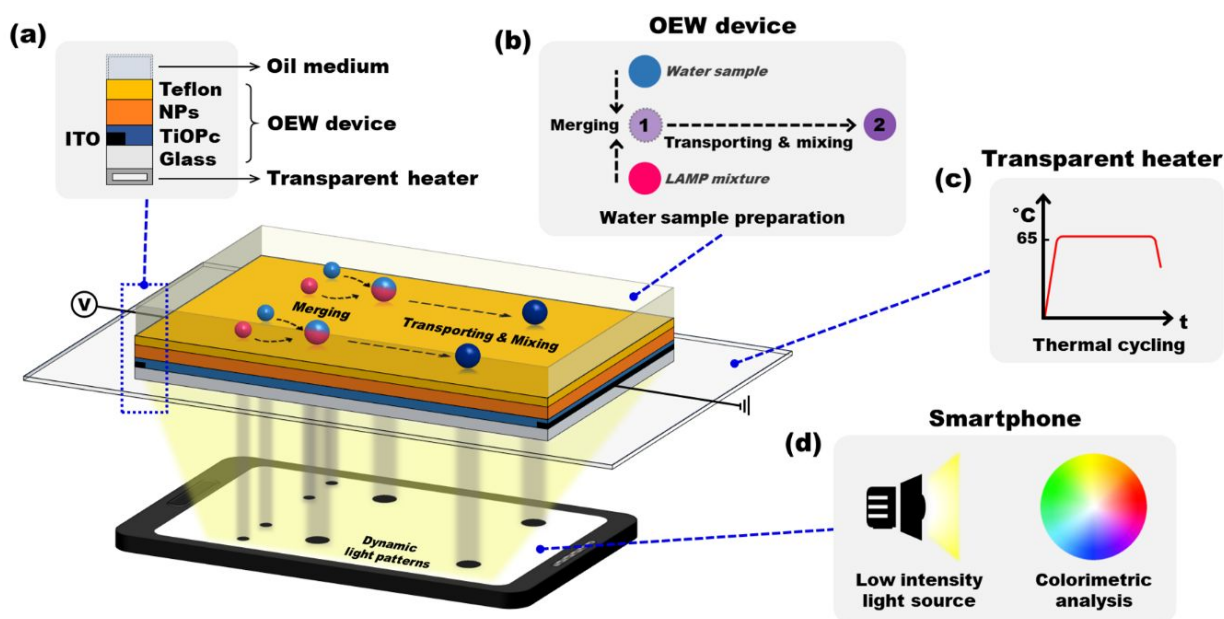


Fig. 17 A lab-on-a-smartphone (LOS) platform for on-site detection of water quality through portable LAMP testing. (a) and (b) The LOS platform that integrates plasmonic-enhanced OEW technology with a transparent heater and a smartphone. The OEW device enables allows on-chip LAMP mixture and water sample preparations with light-driven OEW droplet manipulations, with low-intensity light patterns illuminated by the smartphone below. (c) A transparent heater provides the heating conditions to perform isothermal nucleic acid amplifications for LAMP assays. (d) A smartphone has a secondary function of serving as a portable colorimetric analyzer during the LAMP reaction. The LOS platform can perform rapid assessment of the environmental water samples via LAMP assays without requiring any bulky and sophisticated laboratory equipment or skilled personnel. Reproduced with permission from Ref. ⁵⁵.

throughout the entire duration of the LAMP reaction using a smartphone's digital camera. The positive LAMP assay showed the color of the reaction mixture gradually changed from pink to yellow, indicating a successful DNA amplification. Using the smartphone's app, this colorimetric observation was further quantified via the time-dependent RGB-based analysis. A distinct difference in its RGB values was quantitatively indicated to validate the successful amplification of the target DNA sequence.

A SCOEW device can perform on-chip sample preparation effectively with multiplexed droplet manipulation functions. The integration of a smartphone with the OEW technology promises a simple yet powerful, portable LOS platform that can be greatly beneficial for numerous environmental applications. This LOS platform is potentially useful for in-situ microbiological monitoring of environmental water due to its ability to deliver rapid and reliable test results in resource-limited settings without requiring any bulky and complex laboratory equipment or skilled personnel.

6. Conclusion and outlook

OEW technologies have been emerging as solutions for effective light-driven droplet manipulations with the benefits of device functionality, reconfigurability, adaptability, and cost effectiveness and showing great promises for various lab-on-a-chip applications. This review paper presents the fundamentals,

research progresses and innovations of OEW technologies. Conventional OEW-based devices can be categorized into: (1) early-stage OEW, (2) COEW, and (3) o-OEW. These OEW-based devices have a similar droplet actuation principle, whereby the optical addressing onto a photoconductive surface modifies its electrical impedance and shifts majority of the voltage drop to the dielectric layer to induce a localized electrowetting effect. In early-stage OEW devices, a liquid droplet is sandwiched between two parallel plates, with the bottom plate consisting of an OEW surface and an array of 2D patterned electrodes. However, it has several drawbacks, including complexity in device fabrication and difficulty of interfacing with other microfluidic components. In COEW, the patterned electrodes have been replaced by a continuous (featureless) photoconductive layer, where virtual electrodes can be created on the photoconductive layer upon light illumination. This allows continuous transportation of liquid droplets and eliminates the issue with droplet size limitation. However, COEW devices still face similar fabrication complexity and interfacing difficulty due to their sandwiched configuration. Such a deficiency was eliminated in o-OEW by adopting an open (single-sided) configuration. Nevertheless, like the conventional OEW, the physically patterned electrodes give rise to the issues of device extensibility and flexibility by limiting the minimum droplet size to be manipulated.

Further innovations to OEW-based devices have been investigated. Notably, the development of the SCOEW

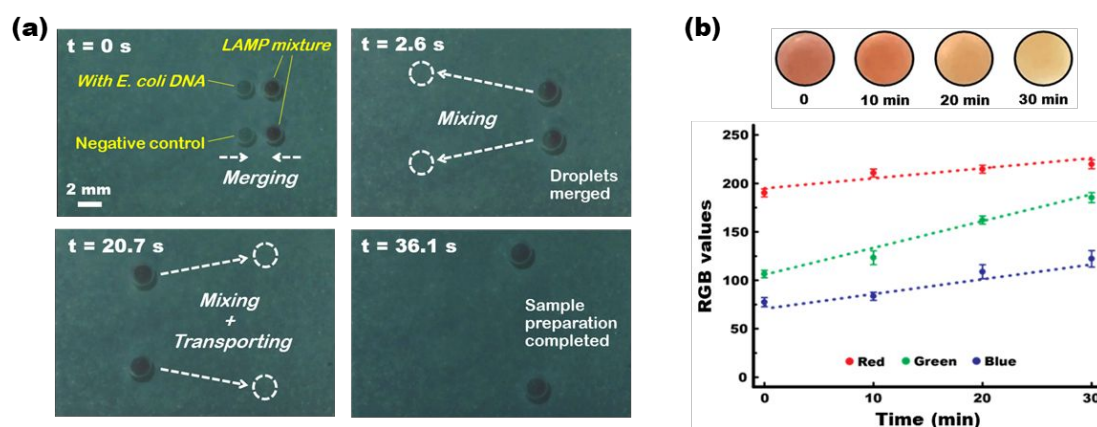


Fig. 18 Experimental demonstrations on the LOS. (a) On-chip *E. coli* sample processing with a 1.0 μL freshwater droplet spiked with *E. coli* DNA and a 1.5 μL droplet of LAMP mixture. (b) LAMP assay results and smartphone-based colorimetric detection. Reproduced with permission from Ref. ⁵⁵.

eliminates the limitations due to its single-sided open configuration structure, continuous photoconductive layer, and no pixelated electrodes. The lateral field modulation in the SCOEW allowed the use of low-intensity light sources such as an LCD display for optical droplet manipulations without any additional optical components. Next, the introduction of the flexible SCOEW technology, which utilized the polymer-based TiOPc as a spin-coatable photoconductive material, offers several benefits over previous OEW devices, such as low-cost simple device fabrication, device flexibility and functionality by allowing light-driven 3D droplet manipulations on a flexible substrate. Additionally, the use of plasmonic nanoparticles further enabled to improve OEW performance by enhancing light absorption and photo-state conductivity of the TiOPc layer. The plasmonic-enhanced SCOEW technology has demonstrated improvement in droplet actuation speed by as much as 39 folds.

With the benefit of effective optical droplet manipulation, recent progresses have seen OEW devices being incorporated with commercially available smartphones. Not only was a smartphone's display used as a portable, programmable, and low-intensity light source for automated OEW droplet manipulations, but also the vast capabilities of a smartphone and its wide range of mobile apps allow it to work as an optical detector or a convenient tool for instant wireless communication of the detected information. Such capabilities enable smartphone-integrated OEW devices to be reliable and portable environmental sensors. This paper further reviews the plasmonic-enhanced OEW device integrated with a smartphone, which has been developed as portable biosensors that are capable of performing accurate fluorescence microscopic detection harmful algae cells as well as LAMP assays for rapid and in-situ monitoring of fecal contamination in environmental waters.

Although the OEW technology has shown great promises for potential LOC applications, it still has room for even further developments if given considerable time and efforts. More research efforts can be made to further improve several aspects

of the OEW technology, including low-cost fabrication techniques, reliable device operation, and effective droplet manipulation with low voltage and low power optics requirements. Likewise, the OEW technology can be further optimized to allow parallel manipulations of even larger arrays of liquid droplets, thereby massively boosting its functionality in environmental sensing applications. Moreover, by continuously tapping into the vast capabilities of a smartphone, the smartphone integrated OEW technology has the potential to develop into low-cost, portable biosensors for a broad range of future environmental and biomedical applications.

Author Contributions

Conceptualization: S.K. Thio, S.-Y. Park, funding acquisition: S.-Y. Park, supervision: S.-Y. Park, visualization: S.K. Thio, S.-Y. Park, writing – original draft: S.K. Thio, writing – review & editing: S.-Y. Park.

Conflicts of interest

There are no conflicts to declare.

Acknowledgements

This work was partially supported by the NSF CAREER Award (ECCS - 2046134), USA.

References

- 1 E. Brouzes, M. Medkova, N. Savenelli, D. Marran, M. Twardowski, J. B. Hutchison, J. M. Rothberg, D. R. Link, N. Perrimon and M. L. Samuels, *Proceedings of the National Academy of Sciences of the United States of America*, 2009, **106**, 14195-14200.

- 2 S.-Y. Park, S. Kalim, C. Callahan, M. A. Teitell and E. P. Y. Chiou, *Lab on a chip*, 2009, **9**, 3228–3235.
- 3 A. Huebner, S. Sharma, M. Srisa-Art, F. Hollfelder, J. B. Edel and A. J. deMello, *Lab on a Chip*, 2008, **8**, 1244–1254.
- 4 S.-Y. Park and P.-Y. Chiou, *Advances in OptoElectronics*, 2011.
- 5 J. Wang, J. Wang, L. Feng and T. Lin, *RSC Advances*, 2015, **5**, 104138–104144.
- 6 J. A. Olzmann and P. Carvalho, *Nature Reviews Molecular Cell Biology*, 2019, **20**, 137–155.
- 7 S.-Y. Park, T.-H. Wu, Y. Chen, M. A. Teitell and P.-Y. Chiou, *Lab on a Chip*, 2011, **11**, 1010–1012.
- 8 N. Wen, Z. Zhao, B. Fan, D. Chen, D. Men, J. Wang and J. Chen, *Molecules*, 2016, **21**, 881.
- 9 D. M. Headen, J. R. García and A. J. García, *Microsystems & Nanoengineering*, 2018, **4**, 1–9.
- 10 M. Navi, N. Abbasi, M. Jeyhani, V. Gnyawali and S. S. Tsai, *Lab on a chip*, 2018, **18**, 3361–3370.
- 11 S.-Y. Park, T.-H. Wu, Y. Chen, S. Nisperos, J. F. Zhong and P.-Y. Chiou, presented in part at the Proceeding of the 14th International Conference on Miniaturized Systems for Chemistry and Life Sciences (μ TAS 2010), Groningen, Netherlands, October, 2010.
- 12 M. Azizi, M. Zaferani, S. H. Cheong and A. Abbaspourrad, *ACS sensors*, 2019, **4**, 841–848.
- 13 K. Hsieh, K. E. Mach, P. Zhang, J. C. Liao and T.-H. Wang, *Accounts of chemical research*, 2021, 260–266.
- 14 A. M. Kaushik, K. Hsieh and T. H. Wang, *Wiley Interdisciplinary Reviews: Nanomedicine and Nanobiotechnology*, 2018, **10**, e1522.
- 15 S. C. Kim, I. C. Clark, P. Shahi and A. R. Abate, *Analytical chemistry*, 2018, **90**, 1273–1279.
- 16 M. Pellegrino, A. Sciambi, S. Treusch, R. Durruthy-Durruthy, K. Gokhale, J. Jacob, T. X. Chen, J. A. Geis, W. Oldham and J. Matthews, *Genome research*, 2018, **28**, 1345–1352.
- 17 D.-K. Kang, M. M. Ali, K. Zhang, E. J. Pone and W. Zhao, *TrAC Trends in Analytical Chemistry*, 2014, **58**, 145–153.
- 18 Y.-C. Tan, K. Hettiarachchi, M. Siu, Y.-R. Pan and A. P. Lee, *Journal of the American Chemical Society*, 2006, **128**, 5656–5658.
- 19 C. Frey, K. Göpfrich, S. Pashapour, I. Platzman and J. P. Spatz, *ACS omega*, 2020, **5**, 7529–7536.
- 20 L. Shang, Y. Cheng and Y. Zhao, *Chemical reviews*, 2017, **117**, 7964–8040.
- 21 O. D. Velev, B. G. Prevo and K. H. Bhatt, *Nature*, 2003, **426**, 515–516.
- 22 S.-Y. Park, C. Pan, T.-H. Wu, C. Kloss, S. Kalim, C. E. Callahan, M. Teitell and E. P. Y. Chiou, *Applied Physics Letters*, 2008, **92**, 151101.
- 23 D. Chugh and K. V. Kaler, *Microfluidics and Nanofluidics*, 2010, **8**, 445–456.
- 24 A. R. Wheeler, *Science*, 2008, **322**, 539–540.
- 25 J. Cao, Q. An, Z. Liu, M. Jin, Z. Yan, W. Lin, L. Chen, P. Li, X. Wang and G. Zhou, *Sensors and Actuators B: Chemical*, 2019, **291**, 470–477.
- 26 K. Mogi, S. Adachi, N. Takada, T. Inoue and T. Natsume, *Applied Sciences*, 2019, **9**, 2406.
- 27 T. Lee and S.-Y. Park, *Micromachines*, 2021, **12**, 320.
- 28 Z. Jiao, X. Huang, N.-T. Nguyen and P. Abgrall, *Microfluidics and Nanofluidics*, 2008, **5**, 205–214.
- 29 M. L. Cordero, D. R. Burnham, C. N. Baroud and D. McGloin, *Applied Physics Letters*, 2008, **93**, 034107.
- 30 B. J. Won, W. Lee and S. Song, *Scientific reports*, 2017, **7**, 1–9.
- 31 K. Zhang, Q. Liang, S. Ma, X. Mu, P. Hu, Y. Wang and G. Luo, *Lab on a chip*, 2009, **9**, 2992–2999.
- 32 M. A. Bijarchi, A. Favakeh, E. Sedighi and M. B. Shafii, *Sensors and Actuators A: Physical*, 2020, **301**, 111753.
- 33 G. Huang, M. Li, Q. Yang, Y. Li, H. Liu, H. Yang and F. Xu, *ACS applied materials & interfaces*, 2017, **9**, 1155–1166.
- 34 H. Moon, A. R. Wheeler, R. L. Garrell and J. A. Loo, *Lab on a chip*, 2006, **6**, 1213–1219.
- 35 A. R. Wheeler, H. Moon, C. A. Bird, R. R. Ogorzalek Loo, C.-J. C. Kim, J. A. Loo and R. L. Garrell, *Analytical chemistry*, 2005, **77**, 534–540.
- 36 V. Srinivasan, V. K. Pamula and R. B. Fair, *Analytica Chimica Acta*, 2004, **507**, 145–150.
- 37 C. E. Clement and S.-Y. Park, *Applied Physics Letters*, 2016, **108**, 191601.
- 38 C. E. Clement, S. K. Thio and S.-Y. Park, *Sensors and Actuators B: Chemical*, 2017, **240**, 909–915.
- 39 R. A. Hayes and B. Feenstra, 2003, **425**, 383–385.
- 40 S.-Y. Park and Y. Nam, *Micromachines*, 2017, **8**, 3.
- 41 P. Y. Paik, V. K. Pamula and K. Chakrabarty, *IEEE transactions on very large scale integration (vlsi) systems*, 2008, **16**, 432–443.
- 42 J. Cheng, S. Park and C.-L. Chen, *Solar Energy*, 2013, **89**, 152–161.
- 43 V. Narasimhan, D. Jiang and S.-Y. Park, *Applied Energy*, 2016, **162**, 450–459.
- 44 S. K. Thio, D. Jiang and S.-Y. Park, *Lab on a chip*, 2018, **18**, 1725–1735.
- 45 T. Krupenkin and J. A. Taylor, *Nature Communications*, 2011, **2**, 448.
- 46 Q. Chen, S. J. Oh and M. Burhan, *Applied Energy*, 2020, **269**, 115128.
- 47 P. Y. Chiou, H. Moon, H. Toshiyoshi, C. J. Kim and M. C. Wu, *Sensors and Actuators, A*, 2003, 22–228.
- 48 C. Palma and R. D. Deegan, *Langmuir*, 2018, **34**, 3177–3185.
- 49 S. Arscott, *Scientific Reports*, 2011, **1**, 184.
- 50 D. Jiang and S.-Y. Park, *Lab on a chip*, 2016, **16**, 1831–1839.
- 51 J. Loo, S. N. Pei and M. C. Wu, *Journal of Optical Microsystems*, 2021, **1**, 034001.
- 52 V. Shekar, M. Campbell and S. Akella, presented in part at the 2013 IEEE International Conference on Robotics and Automation, Karlsruhe, Germany, October 2013.
- 53 A. Kumar, H.-S. Chuang and S. T. Wereley, *Langmuir : the ACS journal of surfaces and colloids*, 2010, **26**, 7656–7660.
- 54 T. Thomas and H. N. Unni, *Microfluidics and Nanofluidics*, 2019, **23**, 1–12.
- 55 S. K. Thio, S. W. Bae and S.-Y. Park, *Sensors and Actuators B: Chemical*, 2022, **358**, 131543.
- 56 D. Jiang, S. Lee, S. W. Bae and S.-Y. Park, *Lab on a Chip*, 2018, **18**, 532–539.
- 57 H.-S. Chuang, H.-Y. Ku, F.-T. Li, A. Kumar, J.-C. Wang and K.-C. Wang, in *Essentials of Single-Cell Analysis*, Springer, 2016, pp. 159–194.

- 58 J. K. Valley, S. NingPei, A. Jamshidi, H.-Y. Hsu and M. C. Wu, *Lab on a chip*, 2011, **11**, 1292-1297.
- 59 M. G. Lippmann, *Annales de Chimie et de Physique*, 1875, **5**, 494-549.
- 60 F. Mugele and J.-C. Baret, *Journal of Physics: Condensed Matter*, 2005, **17**, 705-774.
- 61 V. Narasimhan and S.-Y. Park, *Langmuir*, 2015, **31**, 8512-8518.
- 62 J. Varghese, H. Wang and L. Pilon, *Journal of The Electrochemical Society*, 2011, **158**, A1106.
- 63 H. Moon, S. K. Cho, R. L. Garrell and C.-J. Kim, *Journal of Applied Physics*, 2002, **92**, 4080-4087.
- 64 M. G. Pollack, F. Richard B and A. D. Shenderov, *Applied Physics Letters*, 2000, **77**, 1725 - 1726.
- 65 J. Lee, H. Moon, J. Fowler, T. Schoellhammer and C.-J. Kim, *Sensors and Actuators A: Physical*, 2002, **95**, 259-268.
- 66 W. C. Nelson and C.-J. C. Kim, *Journal of Adhesion Science and Technology*, 2012, **26**, 1747-1771.
- 67 F. Saeki, J. Baum, H. Moon, J.-Y. Yoon, C. Kim and R. Garrell, *Polym. Mater. Sci. Eng*, 2001, **85**, 12-13.
- 68 D. Brassard, L. Malic, F. Normandin, M. Tabrizian and T. Veres, *Lab on a chip*, 2008, **8**, 1342-1349.
- 69 J. Gong, *Lab on a chip*, 2008, **8**, 898-906.
- 70 Y.-H. Chang, G.-B. Lee, F.-C. Huang, Y.-Y. Chen and J.-L. Lin, *Biomedical Microdevices*, 2006, **8**, 215-225.
- 71 G. J. Shah, A. T. Ohta, E. P.-Y. Chiou and M. C. Wu, *Lab on a chip*, 2009, **9**, 1732-1739.
- 72 S. H. Byun, J. Yuan, M. G. Yoon and S. K. Cho, *Journal of Micromechanics and Microengineering*, 2015, **25**, 035019.
- 73 Z. Yi, H. Feng, X. Zhou and L. Shui, *Frontiers in Physics*, 2020, **8**, 193.
- 74 P.-Y. Chiou, Z. Chang and M. C. Wu, *Journal of Microelectromechanical systems*, 2008, **17**, 133-138.
- 75 P. Y. Chiou, Z. Chang and M. C. Wu, presented in part at the 2003 12th International Conference on Solid-State Sensors, Actuators and Microsystems (Transducers), Boston, MA, USA, June, 2003.
- 76 P. Chiou, S.-Y. Park and M. C. Wu, *Applied Physics Letters*, 2008, **93**, 221110.
- 77 T.-M. Yu, S.-M. Yang, C.-Y. Fu, M.-H. Liu, L. Hsu, H.-Y. Chang and C.-H. Liu, *Sensors and Actuators B: Chemical*, 2013, **180**, 35-42.
- 78 S. N. Pei, J. K. Valley, S. L. Neale, A. Jamshidi, H.-Y. Hsu and M. C. Wu, presented in part at the 2010 IEEE 23rd international conference on micro electro mechanical systems (MEMS), Hong Kong, China, January 2010.
- 79 H.-S. Chuang, A. Kumar and S. T. Wereley, *Applied Physics Letters*, 2008, **93**, 064104.
- 80 S.-Y. Park, M. A. Teitell and E. P. Chiou, *Lab on a chip*, 2010, **10**, 1655-1661.
- 81 E. Liu, C. Wang, H. Zheng, S. Song, A. Riaud and J. Zhou, *Sensors and Actuators B: Chemical*, 2022, **368**, 132231.
- 82 M. Abdelgawad, S. L. S. Freire, H. Yang and A. R. Wheeler, *Lab on a Chip*, 2008, **8**, 672-677.
- 83 Y. Wang and Y.-P. Zhao, *Soft Matter*, 2012, **8**, 2599.
- 84 H. You and A. Steckl, *Journal of adhesion science and technology*, 2012, **26**, 1931-1939.
- 85 J. B. Chae, S. J. Lee, J. Yang and S. K. Chung, *Sensors and Actuators A: Physical*, 2015, **234**, 331-338.
- 86 D. J. Preston, A. Anders, B. Barabadi, E. Tio, Y. Zhu, D. A. Dai and E. N. Wang, *Applied Physics Letters*, 2016, **109**, 244102.
- 87 T.-C. Chu and Y.-W. Lu, *Micromachines*, 2021, **12**, 1385.
- 88 X. Min and W. S. Kim, *Langmuir : the ACS journal of surfaces and colloids*, 2020, **36**, 14841-14848.
- 89 S. Jun Lee, S. Lee and K. Hyoung Kang, *Applied Physics Letters*, 2012, **100**, 081604.
- 90 F. Lapierre, Y. Coffinier, R. Boukherroub and V. Thomy, *Langmuir : the ACS journal of surfaces and colloids*, 2013, **29**, 13346-13351.
- 91 A. Merdasi, A. Moosavi and M. Shafii, *Materials Research Express*, 2019, **6**, 086333.
- 92 K. Takeda, A. Nakajima, K. Hashimoto and T. Watanabe, *Surface science*, 2002, **519**, L589-L592.
- 93 S.-K. Fan, H. Yang and W. Hsu, *Lab on a Chip*, 2011, **11**, 343-347.
- 94 H. Yang, W. Hsu and S.-K. Fan, 2008.
- 95 C. Clement, D. Jiang, S. K. Thio and S.-Y. Park, *Materials*, 2017, **10**, 41.
- 96 H. Li, J. Cui, Z. Yan, M. Jin, Y. Zheng, G. Zhou and L. Shui, *Results in Physics*, 2021, **31**, 105042.
- 97 C. Li and H. Jiang, *Micromachines*, 2014, **5**, 432-441.
- 98 J. Ramanujam and A. Verma, *Materials Express*, 2012, **2**, 177-196.
- 99 C.-H. Lee, A. Sazonov and A. Nathan, *Applied Physics Letters*, 2005, **86**, 222106.
- 100 Z. Shen, T. Masuda, H. Takagishi, K. Ohdaira and T. Shimoda, *Chemical Communications*, 2015, **51**, 4417-4420.
- 101 J. Joseph, S. G. Singh and S. R. K. Vanjari, *Materials Letters*, 2017, **197**, 52-55.
- 102 V. Zardetto, T. M. Brown, A. Reale and A. d. Carlo, *Journal of Polymer Science Part B: Polymer Physics*, 2011, **49**, 638-648.
- 103 H.-j. Ni, J.-g. Liu, Z.-h. Wang and S.-y. Yang, *Journal of Industrial and Engineering Chemistry*, 2015, **28**, 16-27.
- 104 A. Uddin and X. Yang, *Journal of nanoscience and nanotechnology*, 2014, **14**, 1099-1119.
- 105 J. A. Bartelt, Z. M. Beiley, E. T. Hoke, W. R. Mateker, J. D. Douglas, B. A. Collins, J. R. Tumbleston, K. R. Graham, A. Amassian and H. Ade, *Advanced Energy Materials*, 2013, **3**, 364-374.
- 106 Z. Tang, W. Tress and O. Inganäs, *Materials today*, 2014, **17**, 389-396.
- 107 S. K. Thio, S. Bae and S.-Y. Park, *Sensors and Actuators B: Chemical*, 2020, **308**, 127704.
- 108 J. Yguerabide and E. E. Yguerabide, *Analytical Biochemistry*, 1998, **262**, 157-176.
- 109 K. Aslan, J. R. Lakowicz and C. D. Geddes, *Current Opinion in Chemical Biology*, 2005, **9**, 538-544.
- 110 S. K. Thio and S.-Y. Park, *Micromachines*, 2022, **13**, 112.
- 111 M. Bai, Q. Zheng, Y. Tian, Z. Zhang, C. Chen, C. Cheng and X. Meng, *Water Research*, 2016, **96**, 217-224.
- 112 C. Ng, T.-H. Le, S. G. Goh, L. Liang, Y. Kim, J. B. Rose and K. G. Yew-Hoong, *PLoS one*, 2015, **10**, e0143123.
- 113 O. Bastidas, *Technical Note-Neubauer Chamber Cell Counting*, 2013, 1-6.
- 114 G. Bakalar, *SpringerPlus*, 2014, **3**, 1-8.
- 115 S. Lee, V. S. L. Khoo, C. A. D. Medriano, T. Lee, S.-Y. Park and S. Bae, *Water Research*, 2019, **160**, 371-379.

ARTICLE

Journal Name

- 116 N. A. Switz, M. V. D'Ambrosio and D. A. Fletcher, *PloS one*, 2014, **9**, e95330.
- 117 S. Lee, S. Thio, S.-Y. Park and S. Bae, *Harmful Algae*, 2019, **88**, 101638.
- 118 S. K. Thio, S. Lee, S. Bae and S.-Y. Park, presented in part at the 2018 International Conference on Optical MEMS and Nanophotonics (OMN), Lausanne, Switzerland, July, 2018.

Table 1: Table of comparison for various OEW technologies and devices

OEW Platform	Droplet size	Light source	Light intensity	Applied voltage & frequency (AC)/ Electric field (DC)	Active chip area	Actuation speed	Reference
Early-stage OEW	1.6 μL	Laser (532 nm)	636 mW/cm^2	200 V_{pp} 500 Hz	1 cm x 1 cm	7 mm/s	Chiou <i>et al.</i> ⁴⁷
Early-stage OEW	0.4 μL	Laser (532 nm)	636 mW/cm^2	200 V_{pp} 500 Hz	1 cm x 1 cm	78 mm/s	Chiou <i>et al.</i> ⁷⁴
COEW	10 – 50 μL	HeNe laser (632 nm)	254 W/cm^2	200 V_{pp} 10 – 30 kHz	Not stated	1 mm/s	Chiou <i>et al.</i> ⁷⁵ Chiou <i>et al.</i> ⁷⁶
COEW	5 nL – 2 μL	Optical projector	1.38 W/cm^2	52 V_{pp} 10 kHz	1.5 cm x 1.1 cm	2 cm/s	Pei <i>et al.</i> ⁷⁸
COEW + OET	12.5 nL (droplet) 10 μm (beads) HeLa cells	Optical projector	1.38 W/cm^2	40 V_{pp} , 10 kHz (OEW) 10 V_{pp} , 200 kHz (OET)	Not stated	8 mm/s (OEW) 60 $\mu\text{m}/\text{s}$ (OET)	Valley <i>et al.</i> ⁵⁸
COEW	4 μL	Optical projector	Not stated	188 V_{pp} 500 Hz	Not stated	39 $\mu\text{m}/\text{s}$	Yu <i>et al.</i> ⁷⁷
o-OEW	Not stated	Laser (670 nm)	15 mW/cm^2	42 V_{rms} 500 Hz	Not stated	3.6 mm/s	Chuang <i>et al.</i> ⁷⁹
o-OEW	1 μL	Optical projector	1.5 W/cm^2	53 V_{rms} 10 kHz	1 cm x 1.5 cm	4.5 cm/s	Loo <i>et al.</i> ⁵¹
SCOEW	250 μL 0.5 μL 50 μL	Optical projector LCD display	Not stated	Not stated (DC)	5 cm (electrode gap)	102 $\mu\text{m}/\text{s}$ 510 $\mu\text{m}/\text{s}$ 17.5 mm/s	Park <i>et al.</i> ⁸⁰
SCOEW	20 μL	Optical projector	1.5 W/cm^2	120 V (DC)	5 cm (electrode gap)	12 mm/s	Shekar <i>et al.</i> ⁵²
SCOEW	8 μL	Optical projector	Not stated	200 V (DC)	2.5 cm (electrode gap)	4.86 mm/s (y-direction)	Liu <i>et al.</i> ⁸¹
Flexible SCOEW	3 μL	Optical projector	13.6 mW/cm^2	30 V/mm (DC)	Not stated	3.3 mm/s	Jiang <i>et al.</i> ⁵⁰
Plasmonic-enhanced SCOEW	1 μL	Optical projector	13.6 mW/cm^2	100 V/mm (DC)	2 cm (electrode gap)	12.5 mm/s (instantaneous speed)	Thio <i>et al.</i> ¹⁰⁷
SCOEW	5 μL	Smartphone	140 $\mu\text{W}/\text{cm}^2$	35 V/mm (DC)	2 cm (electrode gap)	2.5 mm/s	Jiang <i>et al.</i> ⁵⁶
SCOEW	1 μL	Smartphone	140 $\mu\text{W}/\text{cm}^2$	120 V/mm	2 cm (electrode gap)	2 mm/s	Lee <i>et al.</i> ¹¹⁷
Plasmonic-enhanced SCOEW	2.5 μL	Smartphone	140 $\mu\text{W}/\text{cm}^2$	100 V/mm	4 cm (electrode gap)	1.21 mm/s	Thio <i>et al.</i> ⁵⁵